PHYSICAL REVIEW B **103**, 024523 (2021)

Multigap superconductivity at an unconventional Lifshitz transition in a three-dimensional Rashba heterostructure at the atomic limit

Maria Vittoria Mazziotti,[1] Antonio Valletta,[2] Roberto Raimondi,[1] and Antonio Bianconi[3]
[1]*Dipartimento di Matematica e Fisica, Università Roma Tre, via della Vasca Navale, 84 00146 Roma, Italy*
[2]*Italian National Research Council CNR, Institute for Microelectronics and Microsystems IMM,*
via del Fosso del Cavaliere, 100, 00133 Roma, Italy
[3]*RICMASS Rome International Center for Materials Science, Superstripes Via dei Sabelli 119A, 00185 Roma, Italy;*
Institute of Crystallography, CNR, via Salaria Km 29. 300, I-00016 Roma, Italy;
and National Research Nuclear University MEPhI (Moscow Engineering Physics Institute), 115409 Moscow, Russia

(Received 1 November 2020; revised 14 December 2020; accepted 22 December 2020; published 22 January 2021)

It is well known that the critical temperature of multigap superconducting three-dimensional (3D) heterostructures at atomic limit (HAL) made of a superlattice of atomic layers with an electron spectrum made of several quantum subbands can be amplified by a shape resonance driven by the contact exchange interaction between different gaps. The T_C amplification is achieved tuning the Fermi level near the singular nodal point at a Lifshitz transition for opening a neck. Recently high interest has been addressed to the breaking of inversion symmetry which leads to a linear-in-momentum spin-orbit induced spin splitting, universally referred to as Rashba spin-orbit coupling (RSOC) also in 3D layered metals. However the physics of multigap superconductivity near unconventional Lifshitz transitions in 3D HAL with RSOC, being in a non-BCS regime, is not known. The key result of this work getting the superconducting gaps by Bogoliubov theory and the 3D electron wave functions by solution of the Dirac equation is the feasibility of tuning multigap superconductivity by suitably matching the spin-orbit length with the 3D superlattice period. It is found that the presence of the RSOC amplifies both the k dependent anisotropic gap function and the critical temperature when the Fermi energy is tuned near the circular nodal line. Our results suggest a method to effectively vary the effect of RSOC on macroscopic superconductor condensates via the tuning of the superlattice modulation parameter in a way potentially relevant for spintronics functionalities in several existing experimental platforms and tunable materials needed for quantum devices for quantum computing.

DOI: 10.1103/PhysRevB.103.024523

I. INTRODUCTION

It is known that the structure inversion asymmetry (SIA) which stems from the inversion asymmetry of the confining potential in a two-dimensional (2D) electron gas induces a spin-orbit band splitting with states of different helicity [1–9]. Giant spin-orbit induced spin splitting in the range 150–450 meV has been found in metal alloys [10] and transition-metal dichalcogenides [11]. A three-dimensional Rashba spin splitting has been observed in $PtBi_2$, BiTeX (X = Br, Cl, or I), and GeTe which show dispersion along the out-of-plane direction (k_z) [12–14]. The realization of the three-dimensional Rashba-like spin splitting [15] in quantum materials and heterostructures potentially unfolds numerous promising applications. Following the first theoretical study of superconductivity [16] with spin-orbit band splitting in a 2D metallic layer or at the surface of doped WOx oxides, several theoretical works have studied the emergence of superconductivity in the presence of spin-orbit coupling in a 2D metallic layer [17–23].

Recently, experimental evidence that the strength of spin-orbit interaction is correlated with quasi-2D superconductivity in the (111) $LaAlO_3/SrTiO_3$ interface has been reported [24] and confirmed in several systems [25–28]. The spin polarized energy bands near a topological Lifshitz transition can be detected experimentally by ARPES spectroscopy as it has been observed in a complex oxide heterostructure interface [29] and in layered cuprate perovskite superconductors [30]. Today there is a high interest in the physics of quantum complex materials aimed at the realization of mesoscopic quantum heterostructures for novel superconducting Josephson junctions [31,32].

The theoretical studies of superconductivity coexisting with spin-orbit coupling have been limited to a 2D superconducting layer and to a single band metal [16–23], while it is not known how superconductivity will arise in a 3D Rashba system. Moreover, previous theoretical investigations have considered single-gap superconductors while, in multiband 3D superconductors, multiple-gap superconductivity, in the clean limit, need to be considered in the presence of band spin splitting due to spin-orbit coupling.

In fact, in multigap superconductivity, it is no longer possible to neglect the key role of quantum configuration interaction between superconducting gaps as, for example, the BEC-BCS crossover gap at Lifshitz transitions near a band edge and other gaps in the BCS limit far from band edges [33–41]. Finally, all theoretical approaches have been developed in the BCS regime where the Fermi energy is much higher of both the spin-orbit energy band splitting and the energy gap, while the most interesting physics occurs in the regime where the Fermi energy is in the same energy range as the superconducting energy gaps and the spin-orbit splitting.

The main result of this work is the theoretical description of multigap superconductivity [33–42] at the unconventional Lifshitz transition [43] in a 3D heterostructure at the atomic limit with a periodicity of a few nanometers with tunable spin-orbit strength.

We consider a 3D superlattice of metallic layers of thickness L separated by spacers of thickness W and overall periodicity d. Our aim is to show that the interplay between the Rashba spin-orbit coupling (RSOC) and superlattice structure allows for a fine tuning of the critical temperature. To appreciate this point, consider the energy splitting due to the RSOC and the corresponding difference of the Fermi momenta of the two spin eigenstates. This difference introduces a typical SOC length scale l_{SOC}, which may be compared with the modulation of the superlattice d. In a bulk system l_{SOC} can be compared only with the Fermi wavelength, which is typically of the order of 0.1 nm. In contrast in a superlattice, the modulation is of the order of tens of nanometers, which matches the order of magnitude of the RSOC. The RSOC energy is linear in the wave vector $\epsilon \sim \alpha k$, with the constant $\alpha \sim 0.01$ eV nm. By defining $l_{\mathrm{SOC}} = 2\pi\hbar^2/(\alpha m)$, m being the electron mass, one estimates $l_{\mathrm{SOC}} \sim 10$ nm. As a result the tuning of the RSOC may be achieved via the variation of the modulation of the superlattice structure.

The layout of the paper is the following. In the next section we introduce the model Hamiltonian of a 3D layered superconductor in the presence of RSOC. In Sec. III we study the normal phase paying special attention to the topology of the Fermi surface and to the associated features in the single-particle density of states (DOS). In Sec. IV we turn our attention to the superconducting phase where we derive the superconducting gap equation and discuss its numerical solution in the multiband case. Finally, in Sec. V we state our conclusions.

II. THE MODEL

The Hamiltonian of the system under study reads

$$H = H_0 + H_I, \tag{1}$$

where H_0 is the single-particle contribution, which includes the RSOC

$$H_0 = \frac{\mathbf{p}_\parallel{}^2}{2m} + \frac{p_z^2}{2m_z} + V(z) - i\alpha(\sigma_x\hbar\partial_y - \sigma_y\hbar\partial_x). \tag{2}$$

In the above equation, $\mathbf{p} = -i\hbar\nabla$ is the usual momentum operator and $\mathbf{p}_\parallel$ its projection in the xy plane. $V(z) = V(z+d)$ is the periodic potential modeling the superlattice structure $V(z) = -V[\theta(z-d) - \theta(z-L)]$, where $d = L + W$ and V is a positive constant. The single-particle Hamiltonian H_0 has solutions of the form

$$\psi_{n\mathbf{k}\lambda}(\mathbf{r}) = \varphi_{nk_z}(z)\frac{e^{i\mathbf{k}_\parallel\cdot\mathbf{r}_\parallel}}{\sqrt{\mathcal{A}}}\boldsymbol{\eta}_\lambda(\theta), \tag{3}$$

where the wave vector components $\mathbf{k} = (k_x, k_y, k_z) \equiv (\mathbf{k}_\parallel, k_z)$ label plane waves in the xy plane of area $\mathcal{A}$ and the Bloch functions $\varphi_{nk_z}(z)$ along the z axis, n being a subband index. The functions $\varphi_{nk_z}(z)$ and the corresponding eigenvalues are obtained by imposing the continuity of the wave function and its first derivative at the discontinuity points of the potential

$$\varphi(z+d) = e^{ik_zd}\varphi(z), \quad \varphi'(z+d) = e^{ik_zd}\varphi'(z), \tag{4}$$

where the phase factor is required by Bloch's theorem. Finally the effect of the RSOC is encoded in the spinors

$$\boldsymbol{\eta}_\lambda(\theta) = \frac{1}{\sqrt{2}}\begin{pmatrix} 1 \\ i\lambda e^{i\theta}\end{pmatrix}, \quad \lambda = \pm 1, \tag{5}$$

where θ is the angle which defines the direction of the wave vector in the plane $k_x = k_\parallel \cos(\theta)$, $k_y = k_\parallel \sin(\theta)$. As a result the single-particle energies read

$$\epsilon_{n\mathbf{k}\lambda} = \varepsilon_{nk_z} + \frac{\hbar^2 k_\parallel^2}{2m} + \lambda\alpha k_\parallel \equiv \varepsilon_{nk_z} + \varepsilon_{\lambda k_\parallel}. \tag{6}$$

As for the second contribution to the Hamiltonian in Eq. (1) we adopt the standard contact interaction with a cut-off energy $\hbar\omega_0$,

$$H_I = \frac{U_0}{2}\int d\mathbf{r}\Psi_\alpha^\dagger(\mathbf{r})\Psi_\beta^\dagger(\mathbf{r})\Psi_\beta(\mathbf{r})\Psi_\alpha(\mathbf{r}), \tag{7}$$

where $\Psi_\alpha(\mathbf{r})$ is the annihilation fermion field operator and summation over the repeated spin indices (α, β) is understood.

Before considering the superconducting phase in Sec. IV, it is useful to analyze first in the next section the effects of the RSOC in the normal phase and in particular on the density of states. To this end we first consider a simplified tight-binding model and then we turn our attention to the model defined in Eq. (2), by confining to the two lowest subbands for numerical reasons.

For the following discussion it is useful to introduce two dimensionless parameters: the Lifshitz parameter defined as

$$\eta = \frac{\mu - E_2}{\hbar\omega_0} \tag{8}$$

and the rescaled Lifshitz parameter

$$\eta_R = \frac{\mu - E_R}{\hbar\omega_0}, \quad \text{with} \quad E_R = E_2 - \Delta E_{\mathrm{RSOC}}, \tag{9}$$

where μ is the chemical potential which at zero temperature coincides with the Fermi energy, E_2 is the band edge energy of the second subband in the absence of RSOC, ω_0 is the cutoff, and ΔE_{RSOC} is the energy shift due to the RSOC.

III. THE NORMAL PHASE

In the presence of a RSOC, the trend of the DOS can be understood by considering the evolution of the Fermi surface. In this context we will limit our analysis to a two-band system obtained by taking the two lowest subbands.

The starting point is the single-particle energy dispersion (6), which we report here for the sake of clarity:

$$\varepsilon_{n\mathbf{k}\lambda} = \frac{k_\parallel^2}{2m} + \lambda\alpha k_\parallel + \varepsilon_{nk_z}, \tag{10}$$

where for simplicity we adopt units such that $\hbar = 1$.

For both the first and second subband, the energy dispersion along the z axis, which is numerically solved as shown below, can be fitted in terms of a tight-binding model.

In particular, for odd n the agreement is obtained with a two-harmonic expansion, while for n even the agreement is obtained with a three-harmonic expansion. All this can be combined with the observation that, for the purpose of the subsequent discussion, we do not need to specify the precise form of the dispersion along the z axis, but for the fact the ε_{nk_z} increases (for n odd) or decreases (for n even) monotonically between $k_z = 0$ and $k_z = \pi/d$ and, furthermore, is an even function with respect to $k_z \longrightarrow -k_z$, for both even and odd n.

Hence, in order to illustrate the key features of the DOS, we start our analysis with a simplified expression of ε_{nk_z}, namely

$$\varepsilon_{1k_z} = t[1 - \cos(dk_z)], \quad t = 1 \text{ and } 0 < k_z < \pi/d \tag{11}$$

for the first subband and

$$\varepsilon_{2k_z} = t[1 + \cos(dk_z)], \quad t = 1 \text{ and } 0 < k_z < \pi/d \tag{12}$$

for the second subband.

To simplify the notation in the following discussion, the parameters of the in-plane dispersion in Eq. (10) are expressed in units such that $2m = 1$ and we define the spin-orbit typical momentum $k_0 = m\alpha$.

For the sake of definiteness we assume that the minimum energy for the z axis is zero and the maximum is ε_z, i.e., $\varepsilon_{2n+1,0} = 0$ and $\varepsilon_{2n+1,\pi/d} = \varepsilon_z$ for the odd subbands, while we have $\varepsilon_{2n,0} = \varepsilon_z$ and $\varepsilon_{2n,\pi/d} = 0$ for the even subbands. Hence from (10) we take the zero of the energy at the origin in the in-plane momentum space. Thus the dispersion along z for the first and second subband will be equal to $\Delta E_{zn} = \varepsilon_z$.

The quasiparticle energy (10) has axial symmetry so that we may first study it in the $(k_\parallel, k_z)$ plane. From the isoenergetic curves in this plane one can obtain the isoenergetic surfaces by performing a rotation around the k_z axis. At a given chemical potential μ, from the expression of the quasiparticle energy, we derive the values of $k_\parallel$ at fixed k_z and helicity λ,

$$k_\parallel(k_z, \lambda) = -\lambda k_0 \pm \sqrt{k_0^2 + (\mu - \varepsilon_{n,k_z})}, \tag{13}$$

from which we start our discussion. It is useful to distinguish three separate regimes for the Fermi energy: (I) $\varepsilon_z < \mu$; (II) $0 < \mu < \varepsilon_z$; and (III) $-k_0^2 < \mu < 0$, where, in this simplified model, $\Delta E_{\rm RSOC} = -k_0^2$ is the energy shift due to RSOC coupling (see Fig. 1).

Let us examine them in detail.

A. Regime I

When selecting the sign in Eq. (13) we must keep in mind that $k_\parallel \geqslant 0$. Let us start with the helicity $\lambda = 1$. In this case for both even and odd n the only allowed sign is the positive one:

$$k_\parallel(k_z, 1) = -k_0 + \sqrt{k_0^2 + (\mu - \varepsilon_{n,k_z})}. \tag{14}$$

For n odd at $k_z = 0$ one has $k_\parallel(0, 1) = -k_0 + \sqrt{k_0^2 + \mu}$, whereas at $k_z = \pi/d$ one has $k_\parallel(\pi/d, 1) = -k_0 + \sqrt{k_0^2 + (\mu - \varepsilon_z)}$, so that $k_\parallel(\pi/d, 1) < k_\parallel(0, 1)$. Hence the isoenergetic curve, when rotated around the k_z axis, generates a corrugated cylinder wider in $k_z = 0$ and narrower in $k_z = \pm\pi/d$. For n even we have a diametrically opposite situation, i.e., we still have a corrugated cylinder which, however, is narrower in $k_z = 0$ and wider in $k_z = \pm\pi/d$ (Fig. 2).

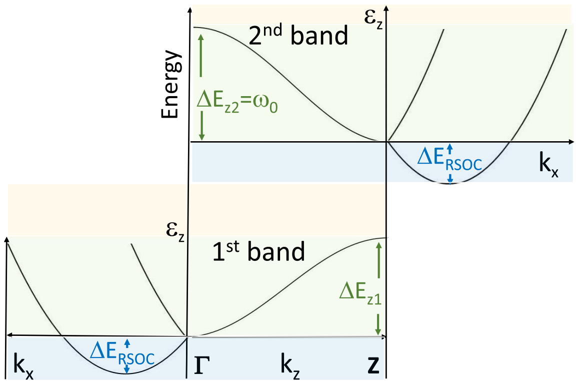

FIG. 1. The dispersion along k_x is shown together with the dispersion along k_z, in arbitrary units, both for n odd (bottom panel) and for n even (top panel). In this figure ΔE_{zn} is the dispersion in the z direction equal to ε_z for both n even and odd (in the numerical model we will assume that ΔE_{z2} is equal to the cut-off energy ω_0). $\Delta E_{\rm RSOC} = -k_0^2$ is, instead, the shift of the Dirac point (defined as the point at which the in-plane dispersions with opposite helicity meet) as a consequence of the dispersion along k_z. The Γ and Z points are the center and the edge of the first Brillouin zone (IBZ). We then indicate the three different regimes in which to study the system: (I) $\varepsilon_z < \mu$ (light-yellow box); (II) $0 < \mu < \varepsilon_z$ (light-green box); and (III) $-k_0^2 < \mu < 0$ (light-blue box).

Let us consider next the case $\lambda = -1$. Since $\mu > \varepsilon_{nk_z}$, the radicand is always greater than k_0, and, therefore, the only allowed sign is the positive one:

$$k_\parallel(k_z, -1) = k_0 + \sqrt{k_0^2 + (\mu - \varepsilon_{n,k_z})}. \tag{15}$$

For n odd at $k_z = 0$, one has $k_\parallel(0, -1) = k_0 + \sqrt{k_0^2 + \mu}$, whereas at $k_z = \pi/d$ one has $k_\parallel(\pi/d, -1) = k_0 + \sqrt{k_0^2 + (\mu - \varepsilon_z)}$. Hence, also in this case, the isoenergetic curve, when rotated around the k_z axis, generates a corrugated cylinder, which is bigger than the previous one.

For n even at $k_z = 0$ one has $k_\parallel(0, -1) = k_0 + \sqrt{k_0^2 + (\mu - \varepsilon_z)}$, whereas at $k_z = \pi/d$ one has $k_\parallel(\pi/d, -1) = k_0 + \sqrt{k_0^2 + \mu}$. Hence, also in this case, the isoenergetic curve, when rotated around the k_z axis, generates a corrugated cylinder, with opposite curvature compared to the case of odd n (Fig. 2).

B. Regime II

Let us begin again by considering first the helicity $\lambda = 1$. Clearly the only sign allowed is the positive one. One notices that exactly at $\mu = \varepsilon_z$ one has $k_\parallel(\pi/d, 1) = 0$, which implies a Lifshitz transition for the Fermi surface. For the energies in this regime we see that not all the values of k_z are allowed. The maximum $k_z = k_z^*$ is determined by the condition $k_\parallel(k_z^*, 1) = 0$, i.e., $k_0 = \sqrt{k_0^2 + (\mu - \varepsilon_{nk_z^*})}$. For odd n, the isoenergetic

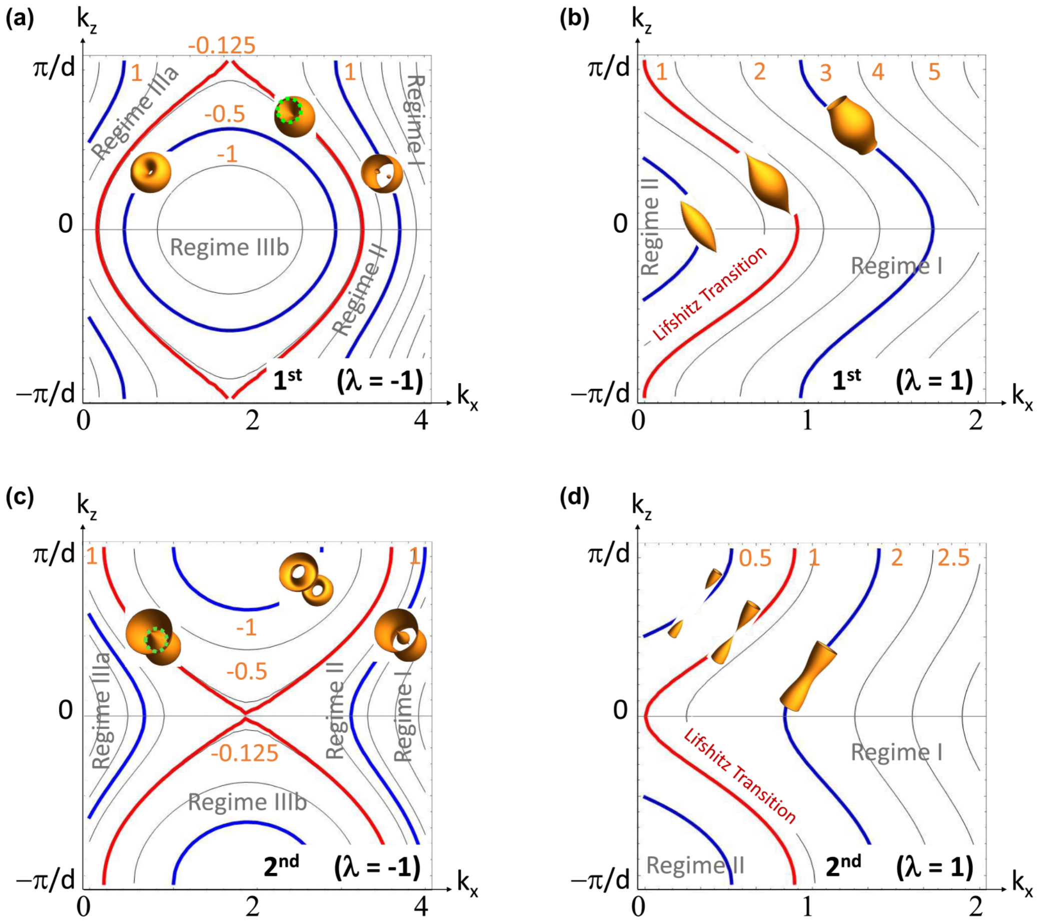

FIG. 2. Top panel: Contour plots in the $(k_\parallel, k_z)$ plane for $\lambda = -1$ (left) and $\lambda = +1$ (right) for a single-harmonic tight-binding model for the first subband of Eq. (11). Parameters are $d = 1, t = 1$ so that $\varepsilon_z = 2$. The RSOC momentum $k_0 = 1.5$. On top of some of the isoenergetic curves are shown the corresponding Fermi surfaces. Bottom panel: Contour plots as above for the second subband of Eq. (12). The orange numbers are the values of the Lifshitz parameter, defined in Eq. (8) of the different level curves, for the choice of the parameters made in this simplified model, while the dashed green curves on the 3D Fermi surfaces of (a) and (c) represent the nodal line of singular points at an unusual van Hove singularity.

curve starts at a point $(0, k_z^*)$ on the k_z axis and ends at a point $k_\parallel(0, 1), 0$ in the $k_\parallel$ axis. The Fermi surface has a fuselike shape (Fig. 2).

For even n, the isoenergetic curve starts at a point $(0, k_z^*)$ on the k_z axis and ends at a point $k_\parallel(\pi/d, 1), \pi/d$ on the $k_\parallel$ axis. In this case, for Fermi surfaces, we obtain half of a spindle that has the tip in (0,0) and reaches the maximum diameter in $k_z = \pi/d$ (Fig. 2).

In this regime the case for helicity $\lambda = -1$ is more complex. The positive sign is of course allowed. The branch with the positive sign starts at the point $(k_\parallel(\pi/d, -1), \pi/d)$ and ends at the point $(k_\parallel(0, -1), 0)$ for odd n, while per even n the positive sign starts at the point $(k_\parallel(0, -1), 0)$ and ends at the point $(k_\parallel(\pi/d, -1), \pi/d)$. In both cases these curves generate corrugated cylinders by rotation around k_z (Fig. 2). For this helicity there is also a possibility of the other branch with the negative sign:

$$k_\parallel(k_z, \lambda) = k_0 - \sqrt{k_0^2 + (\mu - \varepsilon_{n,k_z})}. \tag{16}$$

However this branch is only allowed for a restricted range of k_z values, i.e., $(k_z^*, \pi/d)$ which is the complementary range with respect to that allowed for the other helicity. Hence in this regime of energies the helicity $\lambda = 1$ does not exist for the range $(k_z^*, \pi/d)$, when the helicity $\lambda = -1$ develops another branch exactly in this range. As a result the Fermi surface for the $\lambda = -1$ gets an applelike shape with the poles pushed inwards. This is due to the fact that the points where the phase velocity vanishes are no longer isolated points, but due to the rotation around k_z they form circles with finite measure.

C. Regime III

In this regime there is only the helicity $\lambda = -1$, which however has two branches:

$$k_\parallel(k_z, -1) = k_0 - \sqrt{k_0^2 + (\mu - \varepsilon_{n,k_z})}, \tag{17}$$

$$k_\parallel(k_z, -1) = k_0 + \sqrt{k_0^2 + (\mu - \varepsilon_{n,k_z})}. \tag{18}$$

If $k_0^2 + \mu - \varepsilon_z = 0$, then both branches start at the same point $(k_0, \pi/d)$ for odd n [$(k_0, 0)$ for even n] and from there depart ending at the points $(k_0 + \sqrt{k_0^2 + \mu}, 0)$ and $(k_0 - \sqrt{k_0^2 + \mu}, 0)$

for odd n [$(k_0 + \sqrt{k_0^2+\mu}, \pi/d)$ and $(k_0 - \sqrt{k_0^2+\mu}, \pi/d)$ for even n] in the $k_\parallel$ axis, respectively. This is the case when the singularity in the phase velocity, which in the absence of RSOC is at the isolated point $(0, \pi/d)$ for odd n or $(\pi/d, 0)$ for even n, becomes a finite-measure manifold and develops a van Hove singularity in the DOS (Fig. 2). Hence we may distinguish two cases: (IIIa) $0 < k_0^2 + \mu < \varepsilon_z$ and (IIIb) $0 < k_0^2 + \mu > \varepsilon_z$. In case (IIIa) the argument of the square root is negative, hence the two branches start at a point (k_0, k_z^{**}) with k_z^{**} given by the condition $k_0^2 + \mu = \varepsilon_{nk_z^{**}}$. Then the two branches end on the $k_\parallel$ axis. The Fermi surface generated by these curves has a toruslike shape. In regime (IIIb) instead, the two branches remain disconnected from each other. The Fermi surface has an external and internal part and has a toruslike shape, with the toruses of neighboring zones touching each other (Fig. 2).

Our aim is to evaluate the density of states (DOS) in order to compare it with the detailed calculations made with the more realistic periodic potential model. Therefore, we derive the analytical DOS expression for both helicity values $\lambda = \pm 1$:

$$N_-(\mu) = \frac{1}{2\pi^2}\int_{-k_0}^{\infty} dx(x+k_0) \times \frac{\theta\left(\mu + k_0^2 - x^2\right)\theta\left(x^2 + 2t - \mu - k_0^2\right)}{\sqrt{\left(\mu + k_0^2 - x^2\right)\left(x^2 + 2t - \mu - k_0^2\right)}}, \tag{19}$$

$$N_+(\mu) = \frac{1}{2\pi^2}\int_{k_0}^{\infty} dx(x-k_0) \times \frac{\theta\left(\mu + k_0^2 - x^2\right)\theta\left(x^2 + 2t - \mu - k_0^2\right)}{\sqrt{\left(\mu + k_0^2 - x^2\right)\left(x^2 + 2t - \mu - k_0^2\right)}}, \tag{20}$$

where $x = k_\parallel \mp k_0$ for $\lambda = \mp 1$ and $\theta(x)$ is the Heaviside step function.

Let us analyze the integral defined in Eq. (19) and in Eq. (20). As a function of the variable x, the integrand has singularities at $x = \pm\sqrt{\mu + k_0^2}$ and $x = \pm\sqrt{\mu + k_0^2 - 2t}$. All singularities have index $-1/2$ and hence are integrable. When $\mu + k_0^2 = 2t$, the denominator acquires a zero at the origin. In the absence of spin-orbit interaction, the $1/|x|$ behavior of the denominator is compensated by the numerator and the integral is finite. However, in the presence of spin-orbit interaction, there is a term proportional to k_0 in the numerator and a van Hove singularity develops. The singularity has a logarithmic behavior.

The DOS expression can be computed with Mathematica by using the built-in Heaviside function and numerical integration command. In Fig. 3 are reported the plots of N_-, N_+ (partial DOS), and $N_- + N_+$ (total DOS), respectively, for four values of $k_0 = 0.1,\ 0.2,\ 0.3,\ 0.41,\ 0.5,\ 0.6,\ 0.7,\ 0.8$ and $t = 1$. The partial and the total DOS are reported as a function of the rescaled Lifshitz parameter defined in Eq. (9) where, in this case, $E_2 = 0$, $\Delta E_{\rm RSOC} = -k_0^2$, and $\omega_0 = \Delta E_{z2} = \varepsilon_z = 2t$.

The black curve corresponds to the case when there is no spin-orbit present. Clearly the value $\eta_R = 1$ (in units of t) marks the point of the band edge for the dispersion along the z axis. The spin-orbit interaction develops a van Hove singularity exactly at this point. This behavior, as we will see below, appears in agreement with the more realistic model. This point, $\eta_R = 2t/\Delta E_{z2}$, corresponds to the singularity in the two-dimensional Rashba model at the bottom of the lower band with helicity $\lambda = -1$. In the 3D case the singularity appears at the edge of the band due to the motion along z.

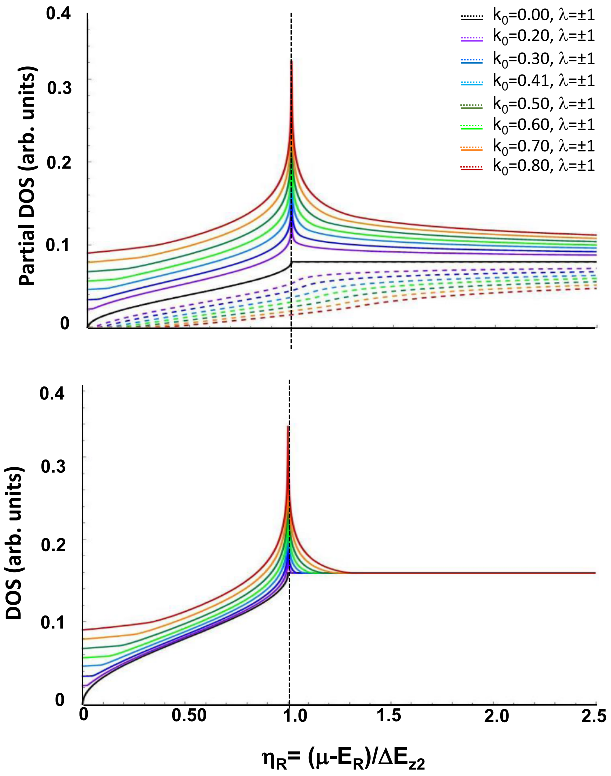

FIG. 3. Total and partial DOS as a function of η_R [Eq. (9)]. Top panel: The partial DOS N_- [Eq. (19)] and N_+ [Eq. (20)] as a function of the rescaled Lifshitz parameter η_R. The black curve is $k_0 = 0$. The other curves have increasing values of $k_0 = 0.1,\ 0.2,\ 0.3,\ 0.41,\ 0.5,\ 0.6,\ 0.7,\ 0.8$. Here $t = 1$. Bottom panel: The total DOS $N_- + N_+$ given in Eqs. (19) and (20) as a function of rescaled Lifshitz parameter η_R. The black curve is $k_0 = 0$. The other curves have increasing values of $k_0 = 0.1,\ 0.2,\ 0.3,\ 0.41,\ 0.5,\ 0.6,\ 0.7,\ 0.8$. Here $t = 1$.

Figure 3 also shows that as k_0 increases, N_- increases while N_+ decreases, in the sum this involves a change only in the proximity of the van Hove singularity. More precisely, while at the Lifshitz transition the partial densities combine to yield a strong change in the DOS, at high energies they compensate, so that the total DOS coincides with the total DOS in the absence of RSOC. This means that in the high-energy limit the parameters of the normal phase and, as we will see below, of the superconducting phase do not depend on k_0, in accordance with the work of Gorkov and Rashba [16].

D. Numerical results for the full model

After the analysis of the simplified tight-binding model, we study the properties of the normal phase starting from the solution of the model of Eq. (2) obtained numerically.

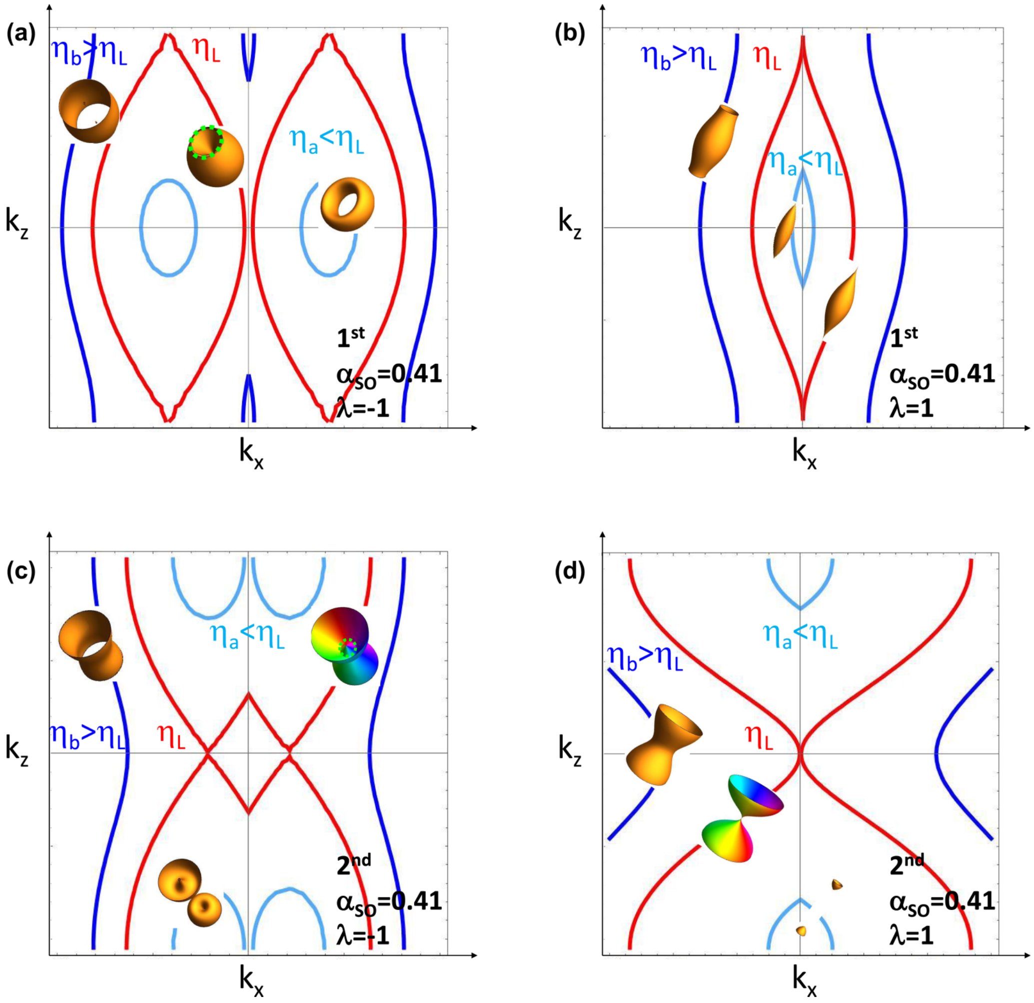

FIG. 4. Isoenergetic curves, Fermi surfaces for the first and second subbands at three different values of Lifshitz parameter. The top panels show the case of $\lambda = 1$ (left) and $\lambda = -1$ (right) for the first subband and for $\Delta E_{\mathrm{RSOC}} = \Delta E_{2z}$ ($\alpha_{\mathrm{SO}} = 0.41$). The bottom panels show the same analysis carried out for the second subband. The DOS maximum is observed at η_L where the system develops a van Hove singularity. In this case the Fermi surface develops a nodal line highlighted in (a) and (c) with a dashed green line. For $\lambda = 1$, both for the first and for the second subband, η_L is independent of the value of α_{SO} and it is equal to -3.9 and 0.92 meV, respectively. While for $\lambda = -1$, η_L changes with α_{SO} (as underlined in Fig. 5), for the first subband $\eta_L = -4.6$ meV, for the second $\eta_L = -0.11$ meV. In (c) and (d), for $\eta = \eta_L$, we highlight the phase factor with the colors of the rainbow and the nodal line (white dashed curve) of the singular points.

For the numerical solution of the normal phase the chosen parameters are: the barrier $V = 0.5$ eV, the thicknesses of the metallic and insulating layers $L = 23$ Å and $W = 7$ Å, respectively, with total periodicity $d = 30$ Å, the effective masses $m = m_z = m_e$, the cut-off energy $\hbar\omega_0 = 30$ meV, and the coupling constant $g = 0.4$.

According to the works [3,6] we express the Rashba coupling constant in the following form:

$$\alpha = 2\frac{\hbar^2}{2m}\frac{2\pi}{d}\alpha_{\mathrm{SO}}, \tag{21}$$

where α_{SO} is a dimensionless parameter which describes the strength of the Rashba momentum in units of the inverse lattice spacing along the z direction.

Similarly to what has been done for the tight-binding model, we carry out the analysis of the evolution of Fermi surfaces for ε_{2k_z} obtained numerically by distinguishing for each of the listed regimes three distinct cases: $\Delta E_{z2} \gtreqqless \Delta E_{\mathrm{RSOC}}$, where $\Delta E_{z2} = \varepsilon_{2k_z,\mathrm{max}} - \varepsilon_{2k_z,\mathrm{min}}$ is the bandwidth of the dispersion along the axis of confinement z in the presence of a potential of the form Kronig-Penney, while in this case $\Delta E_{\mathrm{RSOC}} = E_0 = -(m\alpha^2)/(2\hbar^2)$ is the energy shift due to the RSOC. The model parameters are chosen so that ΔE_{z2} is of the same order of magnitude as the cut-off energy.

This study concerns a two-band system, where the first subband has an s symmetry, while the second one has p symmetry. The results are shown in Fig. 4: in Figs. 4(a), 4(b), 4(c), and 4(d) we plot the isoenergetic curves in the (k_x, k_z) plane for $\lambda = \pm 1$ and for the first and the second subbands versus the Lifshitz parameter η, Eq. (8), where $E_2 = 163.64$ meV is the band edge of the second subband in the absence of RSOC and ω_0 is the cut-off energy for $\hbar = 1$. In this figure we also report the evolution of Fermi surfaces for three distinct values of the parameter η. The analysis is made for $\alpha_{\mathrm{SO}} = 0.41$ value for which the condition $\Delta E_{\mathrm{RSOC}} = \Delta E_{z2} = \omega_0$ is verified. In the case of the second subband for an energy value close

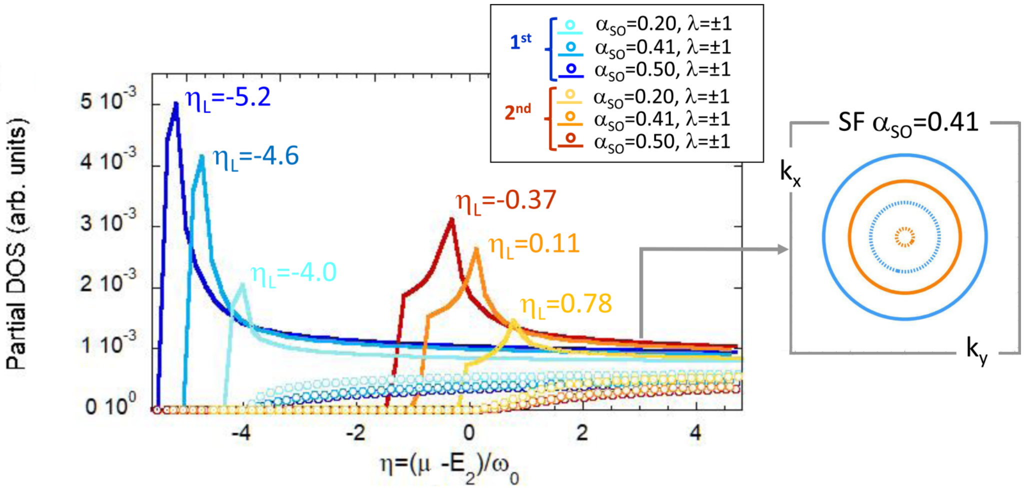

FIG. 5. Partial density of the states vs η and projection of the FS in the plane $(k_x,\ k_y)$ at $k_z = Z$. In the left panel the continuous curves represent the partial DOS for $\lambda = -1$, the dots those for $\lambda = 1$, the shades of blue refer to the first subband for three different values of $\alpha_{\rm SO} = 0.20,\ 0.41,\ 0.50$, while the shades of red to the second subband. The figure shows that the value of η_L, for which the FS have a nodal line (Fig. 4), decreases as $\alpha_{\rm SO}$ increases by an amount equal to E_0/ω_0, while the peak of the partial DOS $\lambda = +1$ increases. In the right panel the light blue curve represents the projection of the FS relative to $\lambda = -1$ in the plane for the first subband, the light blue dashed curve is relative to $\lambda = 1$. Similarly, the orange curves refer to the second subband. This panel is built for $\alpha_{\rm SO} = 0.41$ and $\eta = 3$.

to the van Hove singularity (η_L) we take into account that in the presence of RSOC the spinor [Eq. (5)] and the gap [Eq. (39)] depend on a phase factor $e^{i\vartheta}$ and the removal of the spin degeneration splits the dispersion into two bands with opposite helicity. To take this into account we plot the FS at the Lifshitz transition with a color that varies with ϑ in panels (c) and (d) of Fig 4. In particular, for $\lambda = 1$ it varies from red to purple, while for $\lambda = -1$ it varies from purple to red.

We highlight the three regimes analyzed previously and a change in symmetry in passing from the first to the second subband. Such a change, for the first subband, occurs at the point Γ, origin of the first Brillouin zone (IZB), while, in the second subband, it occurs at the point Z, edge of the IBZ in the z direction. As the Rashba coupling changes ($\Delta E_z \gtreqless \Delta E_{\rm RSOC}$), only a flattening of the contour lines and Fermi surfaces is observed to the left and a shift to the right of the singular points. The latter are the points where the phase velocity vanishes and which generate, for rotation around the k_z axis, circles whose radius increases with $\alpha_{\rm SO}$. The energy in which this van Hove unusual singularity occurs is indicated in the figure with η_L and in the literature it is called neck opening energy. We can note that for the bands with positive helicity η_L is independent of the value of $\alpha_{\rm SO}$, while for the bands with negative helicity it varies as the RSOC varies.

This behavior is confirmed by Fig. 5 where we plot the partial DOS for $\alpha_{\rm SO} = 0.20$ ($\Delta E_{\rm RSOC} > \Delta E_{z2}$), $\alpha_{\rm SO} = 0.41$ ($\Delta E_{\rm RSOC} > \Delta E_{z2}$), and $\alpha_{\rm SO} = 0.50$ ($\Delta E_{\rm RSOC} > \Delta E_{z2}$). In this figure η_L coincides with the value for which the partial DOS relative to $\lambda = -1$ for the first and second subband has a maximum. As you can see, as $\alpha_{\rm SO}$ increases, the η_L parameter decreases while the value of the partial DOS peak $\lambda = -1$ increases. In particular, in the case of the first subband for $\lambda = -1$ $\eta_L = -5.2$ for $\alpha_{\rm SO} = 0.50$, $\eta_L = -4.6$ for $\alpha_{\rm SO} = 0.41$, and $\eta_L = -4.0$ for $\alpha_{\rm SO} = 0.20$. Indeed, in the case of the second subband for $\lambda = -1$ $\eta_L = -0.37$ for $\alpha_{\rm SO} = 0.50$, $\eta_L = 0.11$ for $\alpha_{\rm SO} = 0.41$, and $\eta_L = 0.78$ for $\alpha_{\rm SO} = 0.20$. In the right panel of Fig. 5 we report the projection of the Fermi surfaces in the plane $(k_x,\ k_y)$ at the point Z of the IZB for $\eta = 3$, where we have highlighted the two possible values of helicity with different colors (light blue for $\lambda = -1$ and orange for $\lambda = 1$).

What can be seen from the graphs in Fig. 5 is a peak in the partial DOS, and then in the total DOS, corresponding to an energy value equal to $E_0/\omega_0 = -(m\alpha^2)/(2\omega_0)$ which, as the coupling constant Rashba increases, it increases and shifts to gradually smaller Lifshitz parameter values, and the shift involves only the negative helicity bands. This is underlined in Fig. 6, in which we have reported the normalized band-edge energy E_R in Eq. (9), for the first and the second subband

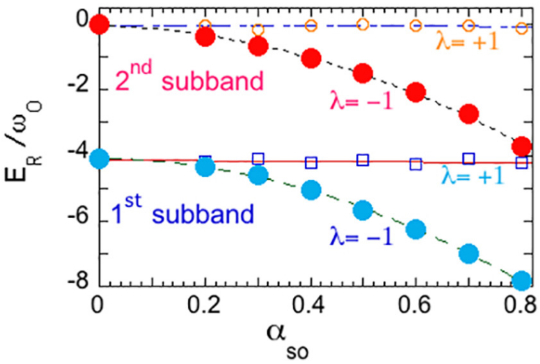

FIG. 6. Normalized band-edge energy as a function of the RSOC constant. The orange empty circles represent the band edge energy vs $\alpha_{\rm SO}$ for the second subband and $\lambda = 1$, while the blue empty squares are relative to the first subband at the same helicity value. The red dots, on the other hand, represent the band edge energy for the second subband at $\lambda = -1$, the light blue dots refer to the first subband for the same helicity value. As noted earlier, a Rashba shift can only be observed for negative helicity bands.

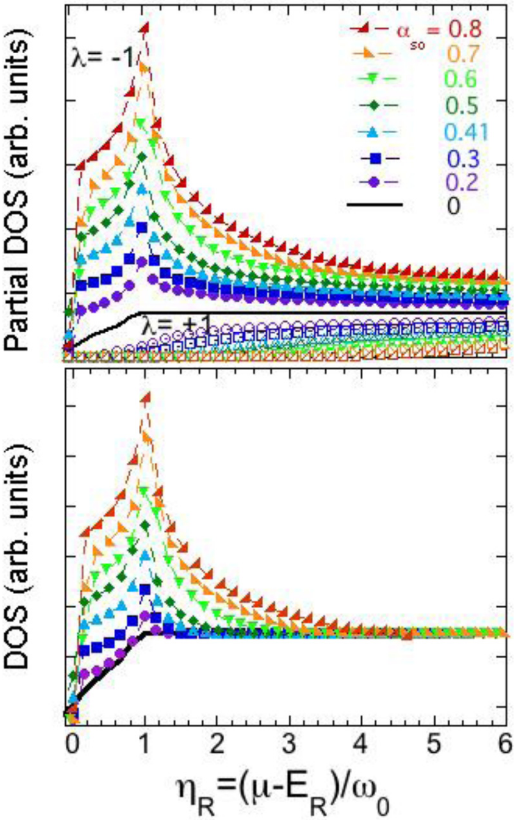

FIG. 7. The DOS for the first and the second subband as the $\alpha_{\rm SO}$ changes. In particular, we have chosen values for this parameter between 0.2 and 0.8 in order to reproduce the three cases previously discussed, $\Delta E_z \gtreqqless \Delta E_{\rm RSOC}$, and compare them with the case of no RSOC, $\alpha_{\rm SO} = 0$. What is observed is that as the RSOC increases, the DOS peak becomes more pronounced and shifts to gradually smaller energies, since the peak occurs at E_0/ω_0.

for the two distinct helicity values as a function of the RSOC constant.

Finally, note that, for the values of the normalized band-edge energy, from this point on we report the results in terms of the rescaled Lifshitz parameter [Eq. (9)].

In the normal phase for a two-band system we plot the total density of the states (DOS) and the partial DOS as the Rashba coupling changes ($\Delta E_z \gtreqqless \Delta E_{\rm RSOC}$) and compare it with the case without RSOC (Fig. 7). In Fig. 7 the DOS is plotted versus the rescaled Lifshitz parameter η_R [Eq. (9)] for different values of $\alpha_{\rm SO}$.

In the case of positive helicity the DOS trend is that of a sloped step, very similar to the trend observed in the absence of RSOC, while in the case of negative helicity we can observe a peak in the density of the states and a shift of the latter towards the left as the parameter $\alpha_{\rm SO}$ increases. This confirms what has been commented for Figs. 2, 3, 4, and 5, or that the effects of a Rashba spin-orbit coupling become more marked for the negative helicity subband.

In a generic 3D system with free-electron-like dispersion relation, the DOS behaves as the square root of energy, whereas in a quantum layer (2D) the DOS is constant and so that it jumps sharply every time a new quantum number from a new layer takes over. In the present case, the DOS shows almost a 2D-like behavior for the first subband. In fact, these are nearly pure 2D subbands with a negligible transversal hopping between the layers. Instead, at the bottom of the second subband appears a sharp step due to contribution of the partial density of states of the second subband to the total density of states. The total energy dispersion of the second subband ΔE_{z2} determines the energy separation between the top and the band edge energy for the second subband. In the energy range $\eta_{\rm 2edge} < \eta < \eta_{\rm 2top}$ (where $\eta_{\rm 2edge}$ and $\eta_{\rm 2top}$ are, respectively, the Lifshitz parameter at the edge and at the top of the second subband), the electronic structure is like that of an anisotropic 3D electron gas, while the 2D character appears at higher energy $\eta > \eta_{\rm 2top}$.

The observed Rashba shift can be understood by considering the simplified model previously introduced. In the absence of RSOC the vanishing of the energy gradient occurs in an isolated point and, therefore, there are no singularities in the DOS. In contrast in the presence of RSOC, the energy gradient vanishes at finite values of the absolute values in-plane momentum $k_\parallel$, therefore we have singular points distributed on circumferences that generate van Hove peaks in the DOS. As the RSOC increases, the energy at which van Hove peaks occur moves to the left, but, as underlined in the discussion of the tight-binding model, the difference in energy between the band edge and the maximum DOS value remains constant and equal to the dispersion along z.

The shape of the Fermi surface is crucial for understanding the electronic properties of metals. As first noticed by Lifshitz [44], changes in the Fermi surface topology cause anomalous behavior of thermodynamic, transport, and elastic properties of materials. Intuitively, the simplest way to observe such an electronic topological transition, also known as Lifshitz transition, is by tuning the Fermi level to the singular point in the band structure where the change of topology takes place. This requires considerable variations of the electron density. A quantum critical point appears in the proximity of a Lifshitz transition with typical quantum criticalities and possible quantum tricritical behavior in itinerant electron systems.

There are two types of Lifschitz transition: type I, the appearing of a new detached Fermi surface region or appearing or disappearing of a new Fermi surface (FS) spot, and type II, the disrupting or the neck-collapsing type of Lifschitz transition with a change of dimensionality that can be induced by orbital symmetry breaking in lightly hole doped bands. In Fig. 4 we show that a new 3D FS opens when the chemical potential crosses the band edge energy, and the electron gas in the metallic phase undergoes an electronic topological transition (ETT). When the chemical potential is beyond the band edge in an anisotropic system at a higher energy threshold, the electronic structure undergoes a second ETT, the 3D-2D ETT, where the FS changes topology from 3D to 2D or vice versa, called also the opening or closing of a neck in a tubular FS or neck collapsing. This ETT is a common feature of all existing high-temperature superconductors and novel materials synthesized by material design in the search for room temperature superconductivity.

However, the analysis made in this section highlights some surprising results, the first is that there is a change in symmetry of the evolution of the FS topology in passing from the first to the second subband. The second is that in the proximity of a type II Lifshitz transition we have a curve of critical points and no longer an isolated point, a fact which explains the appearance of a very pronounced peak in DOS values. The radius of this curve increases with the intensity of the RSOC and this is reflected in an increase and at the same time a true right shift of the DOS maximum. In this situation, the variation in the Fermi surface (FS) topology is absolutely nontrivial.

Clearly we want to see how the above features of the electron spectrum and DOS are reflected in the properties of the superconducting phase. Therefore, after having analyzed in detail the structure of the FS and the DOS in the normal phase, we turn, in the next section, to the study of the superconducting phase.

IV. THE SUPERCONDUCTING PHASE

To investigate how the shape of the Fermi surface and the behavior of the DOS manifest in the superconducting properties of the system with RSOC, we first derive the equations for computing the energy gap. The approach used is the one originally introduced by Innocenti *et al.* [36] and successively developed in Refs. [37–42], where the Bogoliubov equations are solved analytically and numerically without the typical approximations of the BCS theory. The entirely new thing in the following discussion, however, consists of using nonrelativistic Dirac wave functions in order to take into account the additional spin degree of freedom.

The field operators of Eq. (7) can be written in terms of the single-particles states:

$$\psi_{n\mathbf{k}\alpha}(\mathbf{r}) = \varphi_{nk_z}(z)\frac{e^{i\mathbf{k}_\parallel\cdot\mathbf{r}_\parallel}}{\sqrt{\mathcal{A}}}\boldsymbol{\chi}_\alpha \equiv \tilde{\psi}_{n\mathbf{k}}(\mathbf{r})\boldsymbol{\chi}_\alpha, \tag{22}$$

where $\boldsymbol{\chi}_\alpha$ with $\alpha = \uparrow, \downarrow$ are the usual spinors associated with the quantization of the spin along the z axis. This is a legitimate expression for the field operators since the functions $\psi_{n\mathbf{k}\alpha}(\mathbf{r})$ are the eigenfunctions of the Hamiltonian H_0 obtained by setting $\alpha = 0$ in Eq. (2), i.e., completely neglecting the Rashba term. If we indicate with $c_{n\mathbf{k}\alpha}$ the operators that destroy a particle in the state (22), then the field operators become

$$\Psi_\alpha(\mathbf{r}) = \sum_{n,\mathbf{k}} \psi_{n\mathbf{k}\alpha}(\mathbf{r})c_{n\mathbf{k}\alpha} \tag{23}$$

and the interaction term can be written as

$$\begin{aligned} H_I =& \frac{U_0}{2}\sum_{\mathbf{k}_1,\mathbf{k}_2,\mathbf{k}_3,\mathbf{k}_4}\sum_{\alpha,\beta} I^{n_1,\mathbf{k}_1;n_2,\mathbf{k}_2}_{n_3,\mathbf{k}_3;n_4,\mathbf{k}_4} \\ &\times\; c^\dagger_{n_1,\mathbf{k}_1,\alpha}c^\dagger_{n_2,\mathbf{k}_2,\beta}c_{n_3,\mathbf{k}_3,\beta}c_{n_4,\mathbf{k}_4,\alpha}, \end{aligned} \tag{24}$$

with the overlap integrals defined by

$$\begin{aligned} I^{n_1,\mathbf{k}_1;n_2,\mathbf{k}_2}_{n_3,\mathbf{k}_3;n_4,\mathbf{k}_4} = \int & \tilde{\psi}^*_{n_1,\mathbf{k}_1}(\mathbf{r})\tilde{\psi}^*_{n_2,\mathbf{k}_2}(\mathbf{r}) \\ &\times \tilde{\psi}_{n_3,\mathbf{k}_3}(\mathbf{r})\tilde{\psi}_{n_4,\mathbf{k}_4}(\mathbf{r})d\mathbf{r}. \end{aligned} \tag{25}$$

The integrals in Eq. (25) appear in the treatment of the superconductive phase transition in the presence of a periodic potential and have been extensively discussed [36]. The operators $a^\dagger_{n,\mathbf{k},\lambda}$ that create a particle in state Eq. (3) are related to the $c^\dagger_{n,\mathbf{k},\alpha}$ operators by an unitary transformation

$$a^\dagger_{n,\mathbf{k},\lambda} = \sum_\alpha c^\dagger_{n,\mathbf{k},\alpha}U_{\alpha,\lambda}(\mathbf{k}), \tag{26}$$

where the matrix element of the change of basis is equal to $U_{\alpha,\lambda}(\mathbf{k}) = \boldsymbol{\chi}^\dagger_\alpha \cdot \boldsymbol{\eta}_\lambda(\theta_{\mathbf{k}_\parallel})$. As a result, the four operator products that appear in the expansion of the right-hand side of Eq. (7) can be written as

$$\begin{aligned} & c^\dagger_{n_1,\mathbf{k}_1,\alpha}c^\dagger_{n_2,\mathbf{k}_2,\beta}c_{n_3,\mathbf{k}_3,\beta}c_{n_4,\mathbf{k}_4,\alpha} \\ &= \sum_{\lambda_1,\lambda_2,\lambda_3,\lambda_4} M_{\lambda_1,\lambda_4}(\theta_{\mathbf{k_1}_\parallel} - \theta_{\mathbf{k_4}_\parallel})M_{\lambda_2,\lambda_3}(\theta_{\mathbf{k_2}_\parallel} - \theta_{\mathbf{k_3}_\parallel}) \\ &\quad \times a^\dagger_{n_1,\mathbf{k_1},\lambda_1}a^\dagger_{n_2,\mathbf{k_2},\lambda_2}a_{n_3,\mathbf{k_3},\lambda_3}a_{n_4,\mathbf{k_4},\lambda_4}, \end{aligned} \tag{27}$$

where we have defined

$$M_{\lambda_1,\lambda_4}(\theta_{\mathbf{k}_{1\parallel}} - \theta_{\mathbf{k}_{4\parallel}}) = \sum_\alpha U^\dagger_{\lambda_1,\alpha}(\mathbf{k}_1)U_{\lambda_4,\alpha}(\mathbf{k}_4), \tag{28}$$

and similarly for $M_{\lambda_2,\lambda_3}(\theta_{\mathbf{k}_{2,\parallel}} - \theta_{\mathbf{k}_{3,\parallel}})$. Since the φ_{n,k_z} are Bloch wave functions, the integral (25) is different from zero only for $\mathbf{k}_1 + \mathbf{k}_2 = \mathbf{k}_3 + \mathbf{k}_4$ and the expression for H_I becomes

$$\begin{aligned} H_I =& \frac{1}{2}\sum_{n_1,n_2,n_3,n_4,\mathbf{k}_1,\mathbf{k}_2,\mathbf{K}} U^{n_1,\lambda_1;n_2,\lambda_2}_{n_3,\lambda_3;n_4,\lambda_4}(\mathbf{k}_1,\mathbf{k}_2;\mathbf{K}) \\ &\times a^\dagger_{n_1,\mathbf{k}_1,\lambda_1}a^\dagger_{n_2,-\mathbf{k}_1+\mathbf{K},\lambda_2}a_{n_3,-\mathbf{k}_2+\mathbf{K},\lambda_3}a_{n_4,\mathbf{k}_2,\lambda_4}, \end{aligned} \tag{29}$$

where the effective potential reads

$$\begin{aligned} & U^{n_1,\lambda_1;n_2,\lambda_2}_{n_3,\lambda_3;n_4,\lambda_4}(\mathbf{k}_1,\mathbf{k}_2;\mathbf{K}) = U_0 I^{n_1,\mathbf{k}_1;n_2,-\mathbf{k}_1+\mathbf{K}}_{n_3,-\mathbf{k}_2+\mathbf{K};n_4,\mathbf{k}_2} \\ &\times M_{\lambda_1,\lambda_4}(\theta_{\mathbf{k}_{1\parallel}} - \theta_{\mathbf{k}_{2\parallel}})M_{\lambda_2,\lambda_3}(\theta_{-\mathbf{k}_{1\parallel}+\mathbf{K}_\parallel} - \theta_{-\mathbf{k}_{2\parallel}+\mathbf{K}_\parallel}). \end{aligned} \tag{30}$$

Equation (29) is the expression of the interaction term when both RSOC and a periodic potential are present. It can be viewed as the *natural* extension to a multiband system of Eq. (4) of [16] and, from this point on, the computation of the superconducting gap follows the same steps. In agreement with Gor'kov and Rashba [16] we assume that the normal and the anomalous Green's functions are diagonal in the helicity base. Hence we consider only Cooper pairs with zero net momentum ($\mathbf{K} = 0$), formed with particles in the same band and with the same helicity $\{(n,\mathbf{k},\lambda), (n,-\mathbf{k},\lambda)\}$, which are connected by the time reversal symmetry operator. We allow for the contact exchange interaction H_I to connect pairs in different bands with different helicity: the pair $\{(n,\mathbf{k},\lambda), (n,-\mathbf{k},\lambda)\}$ can be scattered into the pair $\{(l,\mathbf{q},\nu), (l,-\mathbf{q},\nu)\}$ where n, λ, l, and ν can assume any allowed value. We emphasize that, as discussed in Ref. [16], the existence of a different pairing function in each helicity band implies a mixture of singlet and triplet pairing. Symmetric and antisymmetric combinations (see Eq. (22) of Ref. [16]) of the pairing functions for the two helicity bands correspond to the singlet and triplet component with respect to the original spin quantization axis taken along the z direction. This can be seen by using the transformation (26) connecting the electron operators between the original spin basis and the helicity basis.

Following the *standard* Gor'kov approach at finite temperature, we introduce the Matsubara imaginary time operators

$a_{n,\mathbf{k},\lambda}(\tau)$ that follow the imaginary time evolution equation $-\partial_\tau a_{n,\mathbf{k},\lambda}(\tau) = [a_{n,\mathbf{k},\lambda}(\tau), H]$. In terms of these operators the *normal* $[G_{n,\lambda}(\mathbf{k}, \tau - \tau')]$ and the *anomalous* $[F^\dagger_{n,\lambda}(\mathbf{k}, \tau - \tau')$ and $F^\dagger_{n,\lambda}(\mathbf{k}, \tau - \tau')]$ Green's functions are defined as

$$G_{n,\lambda}(\mathbf{k}, \tau - \tau') \equiv -\langle T_\tau a_{n,\mathbf{k},\lambda}(\tau) a^\dagger_{n,\mathbf{k},\lambda}(\tau')\rangle, \tag{31}$$

$$F^\dagger_{n,\lambda}(\mathbf{k}, \tau - \tau') \equiv \langle T_\tau a^\dagger_{n,-\mathbf{k},\lambda}(\tau) a^\dagger_{n,\mathbf{k},\lambda}(\tau')\rangle, \tag{32}$$

$$F_{n,\lambda}(\mathbf{k}, \tau - \tau') \equiv \langle T_\tau a_{n,-\mathbf{k},\lambda}(\tau) a_{n,\mathbf{k},\lambda}(\tau')\rangle, \tag{33}$$

where T_τ denotes the imaginary-time ordering operator. By using a mean-field approach, we arrive, after a lengthy algebra, to the self-consistent gap equation:

$$\Delta_{n,\lambda}(\mathbf{k}) = -\frac{1}{2}\sum_{l,\mathbf{q},\nu} U'_{n,\lambda;l,\nu}(\mathbf{k},\mathbf{q}) \frac{\Delta_{l,\nu}(\mathbf{q})}{2E_{l,\nu}(\mathbf{q})} \tanh\left(\frac{\beta E_{l,\nu}(\mathbf{q})}{2}\right), \tag{34}$$

where $\Delta_{n,\lambda}(\mathbf{k})$ is defined as

$$\Delta_{n,\lambda}(\mathbf{k}) \equiv \frac{1}{2}\sum_{l,\mathbf{q},\nu} U'_{n,\lambda;l,\nu}(\mathbf{k},\mathbf{q}) F_{l,\nu}(\mathbf{q}, 0^+), \tag{35}$$

and the quasiparticle energy is

$$E_{l,\nu}(\mathbf{q}) = \sqrt{(\varepsilon_{\nu,\mathbf{q}_\parallel} + \varepsilon_{l,q_z} - \mu)^2 + |\Delta_{l,\nu}(\mathbf{q})|^2}, \tag{36}$$

and the pairing potential reads

$$\begin{aligned} U'_{n,\lambda;l,\nu}(\mathbf{k},\mathbf{q}) &\equiv U^{n,\lambda;n,\lambda}_{l,\nu;l,\nu}(\mathbf{k},\mathbf{q};\mathbf{0}) - U^{n,\lambda;n,\lambda}_{l,\nu;l,\nu}(-\mathbf{k},\mathbf{q};\mathbf{0}) \\ &= U_0 I_{n,l}(k_z,q_z)\lambda\nu e^{-i(\theta_{\mathbf{k}_\parallel} - \theta_{\mathbf{q}_\parallel})}, \end{aligned} \tag{37}$$

with the overlap integral

$$I_{n,l}(k_z, q_z) \equiv I^{n,\mathbf{k};n,-\mathbf{k}}_{l,\mathbf{q};l,-\mathbf{q}}. \tag{38}$$

The matrix elements defined in the Eq. (38) depend on the subband index (n and l) and on the wave vector transversal to the layers (k_z and q_z). In the superposition integrals [Eq. (38)] only the dependence on the transverse moment remains, since the wave functions in the plane are plane waves which compensate for the choice made on $\mathbf{K}$. For a periodic potential barrier associated with the superlattice of layers the density histogram of pairing interaction matrix elements between subbands is illustrated in Fig. 8. The intraband (diagonal elements of matrix) and interband (off-diagonal elements of matrix) distributions show different shapes and widths and have a different range of values. In particular, the off-diagonal elements have a probability density function which is about half of the diagonal elements which instead are of the same order of magnitude.

While in Fig. 8 the dependence on the band indices of the exchange integral is highlighted, in Fig. 9 the dependence on wave vectors is highlighted. This last figure clearly shows that the diagonal elements of the matrix defined by the superposition integral are greater than those off-diagonal, whatever the value of the wave vectors. Furthermore, for both the intraband and the interband there is a curve of values of k_z and q_z for which $I_{11} = I_{22}$ and $I_{12} = I_{21}$, whereas on the right of this curve $I_{11} < I_{22}$ and $I_{12} < I_{21}$, the opposite being true on the left.

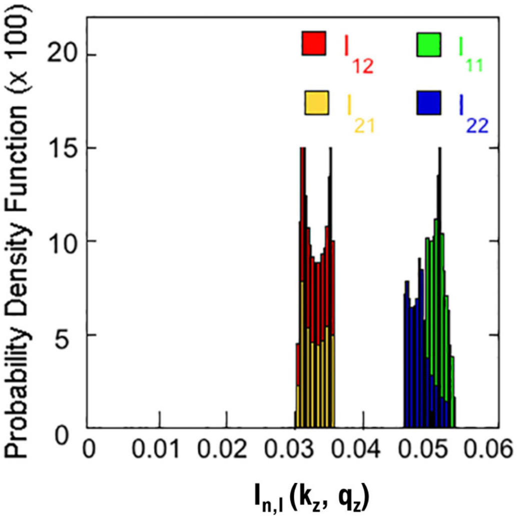

FIG. 8. Histogram of the matrix elements defining the superposition integral of Eq. (38). The green and blue bars refer, respectively, to the intraband pairings $I_{1,1}(k_z, q_z)$ and $I_{2,2}(k_z, q_z)$, while the red and yellow bars refer to, respectively, to the interband couplings $I_{1,2}(k_z, q_z)$ and $I_{2,1}(k_z, q_z)$. The histogram shows a marked anisotropy.

The integral equation (34) shows a dependence of the gap $\Delta_{n,\lambda}(\mathbf{k})$, reminiscent of the Rashba spinors Eq. (5), upon the helicity and the in-plane component of the wave vector through a phase factor $\lambda e^{i\theta_{\mathbf{k}_\parallel}}$. To get rid of this dependence in the self-consistent equation, we define an auxiliary gap function $\Delta_n(k_z)$ as

$$\lambda e^{i\theta_{\mathbf{k}_\parallel}} \Delta_n(k_z) \equiv \Delta_{n,\lambda}(\mathbf{k}). \tag{39}$$

Then the self-consistent equation for $\Delta_n(k_z)$ can be cast in the form

$$\begin{aligned} \Delta_n(k_z) = &-\frac{U_0}{2}\sum_{l,q_z} I_{n,l}(k_z,q_z)\Delta_l(q_z) \\ &\times \sum_\nu \sum_{q_x,q_y} \frac{\tanh\left(\frac{\beta}{2}E_{l,\nu}(\mathbf{q})\right)}{2E_{l,\nu}(\mathbf{q})}, \end{aligned} \tag{40}$$

where it is understood that the wave vector $\mathbf{q}$ appearing in the last term is $\mathbf{q} = (q_x, q_y, q_z)$. The solution of Eq. (40) is

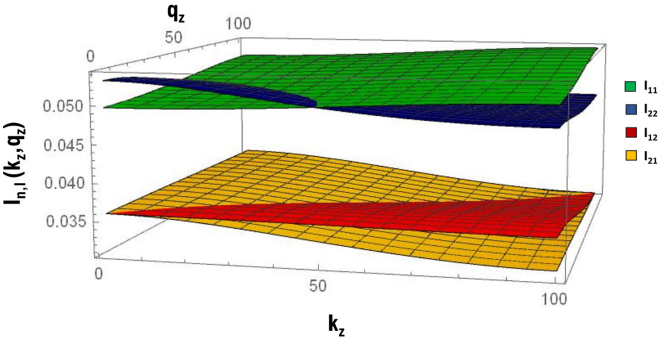

FIG. 9. Terms of the matrix of the exchange integral defined in Eq. (38) as a function of the wave vectors in the direction of the confinement potential. The green plan corresponds to $I_{1,1}(k_z, q_z)$, the blue plan corresponds to $I_{2,2}(k_z, q_z)$, the red plan corresponds to $I_{1,2}(k_z, q_z)$, and the yellow plan corresponds to $I_{2,1}(k_z, q_z)$.

obtained numerically by starting with a guess for $\Delta_n(k_z)$ and iterating until convergence is reached. Since the computational effort is considerable, it becomes important to speed up the calculations by reducing the dimensionality of the summations. In fact, once q_z has been fixed, the argument of the last sum depends on $q_\parallel$ only trough the in-plane dispersion energy $\varepsilon_{\nu,q_\parallel}$. It is then convenient to define a *partial* density of states $g_\nu(\varepsilon_\parallel)$ that allows a transformation of the double sum in Eq. (40) into a one-dimensional integral:

$$\sum_{q_x,q_y} f(\varepsilon_{\nu,q_\parallel}) = \frac{\mathcal{A}}{4\pi^2}\int_{\varepsilon_{\parallel,\min}}^{\varepsilon_{\parallel,\max}} g_\nu(\varepsilon_\parallel) f(\varepsilon_\parallel) d\varepsilon_\parallel. \tag{41}$$

The integration extrema $\varepsilon_{\parallel,\min}$ and $\varepsilon_{\parallel,\max}$ are computed by introducing the contact interaction energy cutoff in the sense that the condition $\varepsilon_{\parallel,\min} < \varepsilon_\parallel < \varepsilon_{\parallel,\max}$ implies the inequality $|\varepsilon_\parallel + \varepsilon_{l,q_z} - \mu| < \hbar\omega_0$.

It is worth to point out that $g_\nu(\varepsilon_\parallel)$ cannot be formulated as a single analytical function but it has to be defined with a piecewise expression that reflects the topology change of the Fermi surface when switching from one regime to another (see Secs. III A, III B, and III C). In fact, the expression defining the partial density of states is

$$\begin{aligned} \frac{\mathcal{A}}{4\pi^2} g_\nu(\varepsilon_\parallel) &= \sum_{q_x,q_y} \delta(\varepsilon_\parallel - \varepsilon_{\nu,\mathbf{q}_\parallel}) \\ &= \frac{\mathcal{A}}{4\pi^2}\int_0^\infty 2\pi \mathbf{q}_\parallel \delta(\varepsilon_\parallel - \varepsilon_{\nu,q_\parallel}) d\mathbf{q}_\parallel, \end{aligned} \tag{42}$$

where the double sum has been transformed in a integral in polar coordinates in the last line. This leads to the following expression for $g_\nu(\varepsilon_\parallel)$:

$$g_\nu(\varepsilon_\parallel) = \begin{cases} 4\pi m \frac{-2\nu k_0}{\sqrt{2m\varepsilon_\parallel + k_0^2}} & \text{if } -\frac{k_0^2}{2m} \leqslant \varepsilon_\parallel < 0,\ \nu = -1, \\ 4\pi m \frac{\nu k_0 + \sqrt{2m\varepsilon_\parallel + k_0^2}}{\sqrt{2m\varepsilon_\parallel + k_0^2}} & \text{if } \varepsilon_\parallel > 0, \\ 0 & \text{otherwise}, \end{cases} \tag{43}$$

where k_0 is defined as in the discussion preceding Eq. (13), but this time we do not set $2m = 1$.

Equation (40) has been solved both in the limit $T \to 0$ (that is $\beta \to \infty$) and in the limit $T \to T_C$ [that is $\Delta_n(k_z) \to 0$ for every n and k_z]. The first limit allows us to determine the gaps while the second allows us to determine the critical temperature.

The results of the numerical computations for the gaps are shown in the Fig. 10(a), in which we plot both partial DOS and $\Delta_n(k_z)$ for the first and second subbands in $k_z = \pi/2d$ as a function of the Lifshitz parameter rescaled η_R [Eq. (9)]. The numerical values of the shift due to the Rashba coupling are indicated in the various panels which differ in the value of the α_{SO} parameter. Furthermore, in this discussion we set the value of the superconducting coupling at $g = 0.4$, where g is defined as $g = g_{3\text{D}}(\mu)U_0$ with $g_{3\text{D}} = \frac{1}{(2\pi)^2(\sqrt{\hbar^2/2m})^3}\sqrt{\mu}$ being the DOS at the Fermi level for a homogeneous system (no RSOC, no peridodic potential along z). In the numerical simulation we assume that g is a constant, so as the chemical potential changes both $g_{3\text{D}}$ and U_0 are continuously recalculated.

We emphasize that, in order to have the full gap, i.e., $\Delta_{\lambda n}(\mathbf{k})$, we must also consider the dependence on the phase factor and on the helicity, for this purpose we keep in mind Fig. 5.

Figure 10(a) shows that both for the gap of the first subband (Δ_1) and for the gap of the second subband (Δ_2) it is possible to distinguish three distinct regimes of multigap superconductivity as a function of the rescaled Lifshitz parameter when it is tuned around the unusual van Hove singularity: an antiresonance regime in which the gaps reach a minimum value for $\eta_R < \eta_L$, where η_L is the value of the van Hove energy for which the DOS shows a peak, a resonance regime for $\eta_R = \eta_L$ in which the gaps reach their maximum value, and, finally, a multiband BCS-like regime for $\eta_R > \eta_L$.

In particular, it can be observed that Δ_1 has a minimum when the chemical potential is near the bottom of the second subband. The partial DOS relative to the first subband, both for $\lambda = 1$ and for $\lambda = -1$, does not change as the chemical potential changes, therefore, the presence of such a pronounced minimum may be due to the existence of a Fano-type antiresonance in superconducting gaps. An antiresonance can be due to an interband exchange term that generates interference effects between the wave functions of a single particle by coupling in a nontrivial way the parameters of the superconducting phase relating to different bands. Both the depth and the position of the minimum in the Δ_1 depend on this term.

A minimum in Δ_1 appears below the band edge where the DOS of the second subband changes abruptly and the Fermi surfaces, as seen above, are in a Lifshitz transition of the first type. That is, the partial filling of the second subband is reflected in the appearance of two new three-dimensional (3D) Fermi surfaces, one for each helicity.

As for the gap of the second subband (Δ_2), Fig. 10(a) shows that it starts to assume nonzero values when the chemical potential has not yet reached the bottom of the second subband. This effect emphasizes, once again, the nonbanal role of interband coupling in a multicomponent system.

Δ_2 reaches the maximum corresponding to the maximum of the partial DOS relative to the second subband and to a negative helicity, i.e., when the chemical potential is near the unusual van Hove singularity, in which the Fermi surfaces changes topology passing from a 3D to a two-dimensional (2D) geometry. As the Rashba parameter α_{SO} varies, as seen previously, the radius of the circumference of the singular points that characterizes the Fermi surface in a Lifshitz transition of the type II (3D-2D ETT) increases, and, as shown in Fig. 10(a), the maximum values of Δ_1 and Δ_2 also increase. By varying the parameter α_{SO}, we distinguish three different regimes: if α_{SO} is such that $\Delta E_{\text{RSOC}} < \Delta E_{z2}$ the maximum of Δ_1 has a value greater than the maximum of Δ_2, for $\Delta E_{\text{RSOC}} = \Delta E_{z2} = \omega_0$ the maxima of the two gaps coincide within the limits of the numerical approximations made, and, finally, for $\Delta E_{\text{RSOC}} > \Delta E_{z2}$ the maximum of Δ_2 exceeds the value of the maximum of Δ_1.

It can also be noted that in the high energy limit the values of the gaps are to a good approximation close to the BCS limit, i.e., in the high energy limit the gaps no longer depend on α [16].

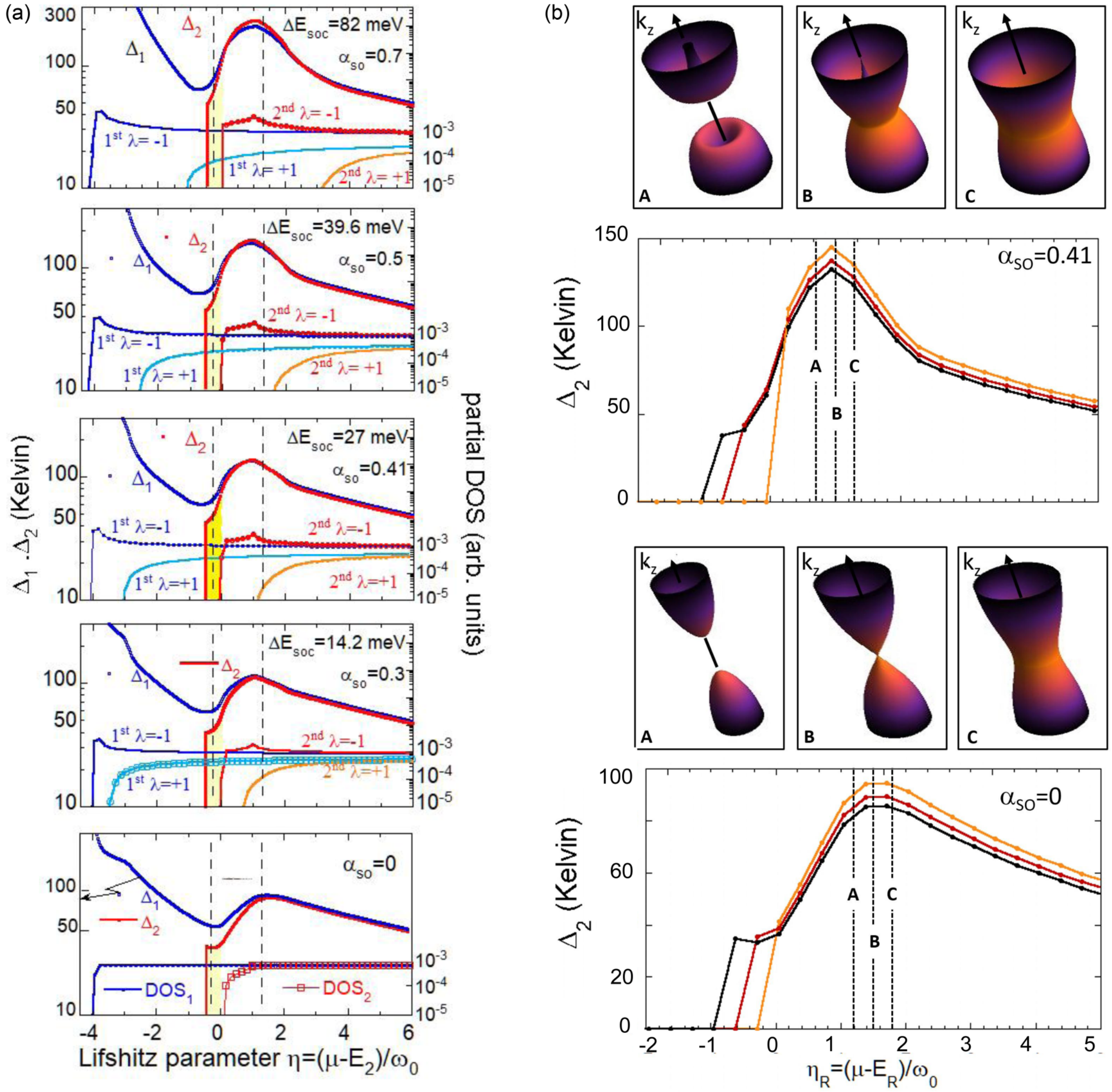

FIG. 10. Properties of the normal phase and the superconductive phase vs the rescaled Lifshitz parameter without and with RSOC for different α_{SO} values such that $\Delta E_{\mathrm{RSOC}} \gtreqless \Delta E_{2z}$. Panel (a) left side Starting from the bottom, the first panel shows the DOS for the first subband (blue curve) and the second subband (red curve) and the trend of the gap relative to the first subband (blue curve) and to the second subband (red curve) as a function of the rescaled Lifshitz parameter. The other panels in (a) are related to the four values of α_{SO} previously discussed, $\alpha_{\mathrm{SO}} = 0.30,\ 0.41,\ 0.50,\ 0.70$, and show the partial DOS for the first subband with positive helicity (light blue curves) and with negative helicity (blue curves) and the partial DOS for the second subband with positive helicity (orange curve) and with negative helicity (red curves). We also report the trend of the gap relative to the first subband (blue curve) and to the second subband (red curve) as a function of the rescaled Lifshitz parameter. An anomalous behavior and an amplification of the parameters of the superconductive phase are observed in a range of rescaled Lifshitz parameter $0 < \eta_R < 1$. That is, in the proximity to the unusual van Hove singularity. Panel (b) right side The values of the gaps for the second subbands at $\alpha_{\mathrm{SO}} = 0$ and $\alpha_{\mathrm{SO}} = 0.41$ vs the rescaled Lifshitz parameter for different values of $k_z = 0,\ \pi/2d,\ \pi/d$ show a variation in a neighborhood of van Hove unusual singularity. We have highlighted the variation of the gap values on the Fermi surface at different k_z for three values of the Lifshitz parameter in $\eta_R = \eta_L$ and $\eta_R = \eta_L \pm 0.5$ by choosing the black color for the low gap values at $k_z = \pi/d$, the red color for $k_z = \pi/2d$, and the orange color for the high gap values at $k_z = 0$.

In Fig. 10(b) we plot the values of Δ_2 as a function of η_R for different values of k_z. It can be observed that Δ_1 does not vary as k_z varies from point Γ to point Z of the IBZ, while it is possible to notice a variation of Δ_2 in a neighborhood of η_L, where the role of exchange integrals [Eq. (25)] becomes crucial.

For values of the Lifshitz parameter close to the van Hove singularity, for the second subband and for a helicity $\lambda = -1$ (the only one present) we plot the corresponding FS highlighting the dependence of Δ_2 from k_z with three different colors from low (black) to high (orange) gap values. In proximity of the unusual van Hove singularity the gap is not constant in k_z since the partial filling of the second subband causes the weight of ε_{l,q_z} in Eq. (36) to be not negligible.

By solving Eq. (40) in the limit $\Delta_n(k_z) \to 0$ we can be compute the critical temperature T_C.

In Fig. 11(a) we plot the values of the critical temperature at different values of the Rashba parameter α_{SO} as a function

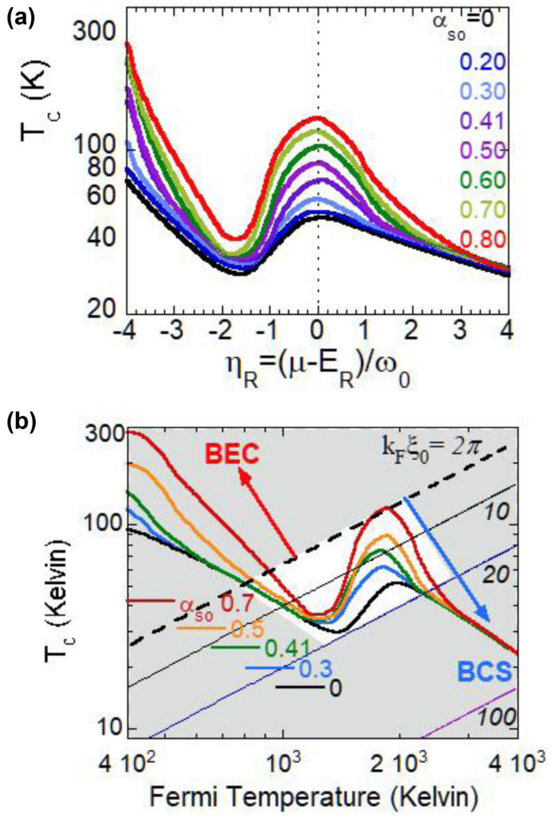

FIG. 11. (a) The critical temperature T_C versus Lifshitz parameter for different values of Rashba coupling α_{SO} on a semilogarithmic scale. The critical temperature appears as an asymmetric function of the Lifshitz parameter and if $\alpha_{\mathrm{SO}} < 0.41$ the maximum of T_C grows slowly, while if $\alpha_{\mathrm{SO}} > 0.41$ it grows faster and faster. (b) In this Uemura plot the critical temperature T_C is plotted on a log-log scale versus the Fermi temperature for different values of Rashba coupling α_{SO}. The white box refers to the Fano resonance appearing near the BEC-BCS crossover indicated by the dashed line.

of the rescaled Lifshitz parameter. The critical temperature appears as an asymmetric function of the Lifshitz parameter regardless of the value of the α_{SO} parameter and shows the typical trend of a Fano antiresonance with a minimum at the first Lifshitz transition and a maximum at the second Lifshitz transition where the Fermi surfaces switch from 3D geometry to 2D geometry. From Fig. 11(a) one can observe that in the presence of RSOC the energies are shifted to the left by an amount equal to $E_0 = -(m\alpha^2)/(2\hbar^2)$ and that the values of the T_C are amplified with respect to the case in which there is no RSOC. In particular, a maximum T_C value is observed in correspondence with the van Hove singularity in the DOS because we have assumed the energy cutoff and the energy dispersion in the z direction to be the same. The BCS theory predicts a value of about 32 K for the critical temperature, with the model parameters chosen in this work, for $\alpha_{\mathrm{SO}} = 0.4$ this value increases about four times.

In Fig. 11(b) we show in a log-log plot the critical temperature T_C as a function of the effective Fermi temperature $T_F = E_F/k_B$ where the Fermi level is calculated from the bottom of the first subband and k_B is the Boltzmann constant. The critical temperature is calculated for different values of the Rashba coupling constant, $\alpha_{\mathrm{SO}} = 0,\ 0.30,\ 0.41,\ 0.50,\ 0.70$. The Fano resonance at the bottom of the second subband occurs in this so called Uemura plot [45] T_C versus T_F. In this figure the dashed line indicates the BEC-BCS crossover predicted to be $T_C = T_F/(k_F\xi_0)$ [46–48]. The Fano resonance clearly occurs on the BCS side of the BCS-BEC crossover where the ratio between T_F and T_C is in the range between 10 and 20. The calculated Fano resonance in the white region occurs on the BCS side up to the largest spin-orbit coupling. In fact the Fano resonance occurs in the range between the BEC crossover and the line $T_C = T_F/20$ in the BCS side. From the figure it can be seen that the critical temperature values remain included in a BCS regime although as α_{SO} increases the Fano resonance appears increasingly shifted towards the BEC limit.

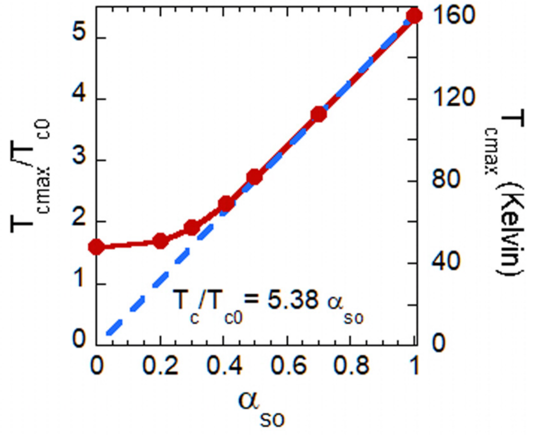

FIG. 12. The maximum value of the critical temperature (red curve) and critical temperature predicted by the BCS theory ratio for different values of α_{SO} parameter. What is observed is a marked amplification of the maximum of the T_C when a Rashba coupling is introduced into the system. In particular, the maximum of the critical temperature increases slowly for $\alpha_{\mathrm{SO}} < 0.41$ and always becomes faster for $\alpha_{\mathrm{SO}} > 0.41$.

Furthermore, it is possible to observe that the value of α_{SO} for which $\Delta E_{\mathrm{RSOC}} = \Delta E_{z2} = \omega_0$, i.e., $\alpha_{\mathrm{SO}} = 0.41$ marks the boundary between two distinct situations: if $\alpha_{\mathrm{SO}} < 0.41$ the maximum of T_C grows slowly, while if $\alpha_{\mathrm{SO}} > 0.41$ it grows faster and faster. All this is highlighted in Fig. 12 in which we report the maximum of the T_C as a function of the Rashba coupling constant (red curve). The maximum of critical temperature increases linearly with RSOC for $\alpha_{\mathrm{SO}} \geqslant 0.41$.

Previously we stressed the fact that near η_L the gaps vary with k_z, this being strongly reflected in the calculation of the gap ratio $2\Delta/T_C$. Therefore, in order to plot this parameter correctly we consider Δ averaged over k_z. So, starting from the bottom of Fig. 13 we plot the gap ratio $2\Delta/T_C$, where T_C is the critical temperature, for the first and the second subband for different values of the α_{SO} parameter as a function of the rescaled Lifshitz parameter.

We observe that the gap ratio differs from the constant value 3.5 foreseen by the BCS theory when the rescaled Lifshitz parameter is closed to $0 < \eta_R < 1$. In particular, the $2\Delta_1/T_C$ ratio for the first subband reaches a minimum, lower than the value predicted by BCS theory, when the rescaled Lifshitz parameter is approximately equal to zero. That is,

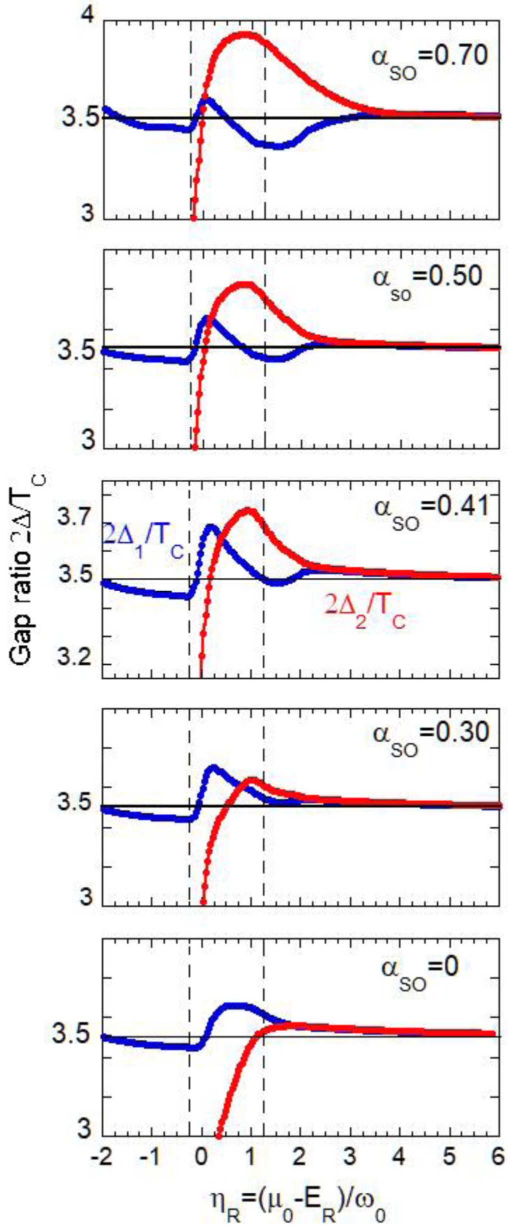

FIG. 13. Properties of the superconductive phase vs the Lifshitz parameter without and with RSOC for different $\alpha_{\rm SO}$ values such that $\Delta E_{\rm RSOC} \gtreqqless \Delta E_{2z}$. This figure shows both the trend of the gap ratio for the first subband (blue curves) and the second subband (red curves) compared to the constant value predicted by the BCS theory (black curves).

when Δ_1 is in an antiresonance regime and the system is close to a Lifshitz transition of the first type. The $2\Delta_1/T_C$ ratio reaches a maximum value for $\eta_R \approx 1$, when the superconducting parameter Δ_1 is in a resonance regime, this occurs close to the type II Lifshitz transition.

Regarding the gap ratio for the second subband $2\Delta_2/T_C$, we observe a significant deviation from the value predicted by the BCS theory in a range of values of the rescaled Lifshitz parameter equal to $0 < \eta < 1$. In particular, when the system is in an antiresonance regime $2\Delta_2/T_C$ diverges, while when Δ_2 is in a resonance regime it shows a maximum. By contrast, such a maximum is not present in the absence of the RSOC as the bottom panel of Fig. 13 shows. As the parameter $\alpha_{\rm SO}$ changes, the maximum of $2\Delta_2/T_C$ increases and, as in the case of Fig. 10, we observe three distinct regimes: when $\Delta E_{\rm RSOC} < \Delta E_{z2}$ we have $2\Delta_2/T_C < 2\Delta_1/T_C$, when $\Delta E_{\rm RSOC} < \Delta E_{z2} = \omega_0$ the two gap ratios intersect, and, finally, for $\Delta E_{\rm RSOC} > \Delta E_{z2}$ we have $2\Delta_2/T_C > 2\Delta_1/T_C$.

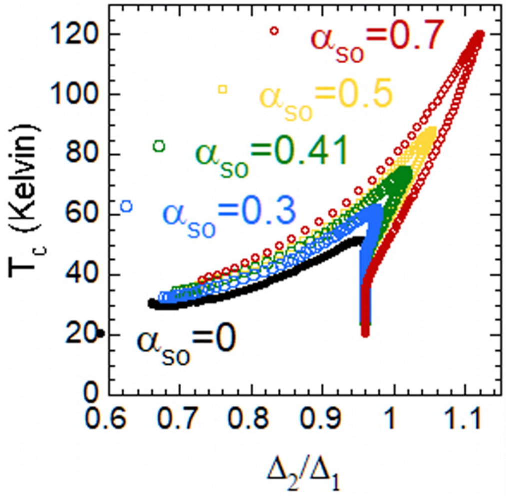

FIG. 14. The trend of the critical temperature vs the Δ_2/Δ_1 ratio for different values of the parameter $\alpha_{\rm SO}$. The T_C trend shows a strong asymmetry which becomes maximum when the Δ_2/Δ_1 ratio is maximum.

We see in Fig. 13 that the gap ratio to the transition temperature $2\Delta_2/T_C < 3.9$ in the second subband, at the maximum critical temperature, in spite of the peak of the partial DOS in the second subband due the van Hove singularity brought about by the largest spin-orbit coupling $\alpha_{\rm SO} = 0.7$, does not show a large deviation from the standard weak coupling universal value 3.52 predicted by the single-band BCS theory. This is in agreement with the corresponding gap ratio $2\Delta_1/T_C = 3.4$ in the first subband. We plot T_C versus the Δ_2/Δ_1 ratio for different values of the parameter $\alpha_{\rm SO}$ in Fig. 14, which shows that Δ_2/Δ_1 ratio is only 1.12, at maximum T_C, for $\alpha_{\rm SO} = 0.7$. Moreover, we want to point out that for $\alpha_{\rm SO} = 0.41$ the gap ratio $\Delta_2/\Delta_1 < 1$ while the ratio between the partial DOS $N_2/N_1 > 1$ due to the van Hove singularity in the second subband. These results show that the present superconducting scenario is in the weak coupling regime where the mean-field approximation is valid. In fact, the aim of this work is to show a scenario with weak electron-phonon coupling, where the amplification of the critical temperature has been driven by interband pairing in the presence of strong spin-orbit coupling. It is well known that in the multigap Bogoliubov superconductivity [49–51] the Δ_2/Δ_1 ratio becomes proportional to N_1/sN_2 where the contact nonretarded-exchange interaction (interband pairing) becomes more relevant that the retarded bosonic exchange pairing. From Fig. 14 we can see a marked anisotropy in the trend of the critical temperature which shows a maximum corresponding to the maximum value of the Δ_2/Δ_1 ratio.

Further work is in progress to study the cooperative role of contact and retarded interactions in anisotropic superconductivity related to the anisotropic k-space pairing in the Fermi surface topology at unconventional Lifshitz transitions.

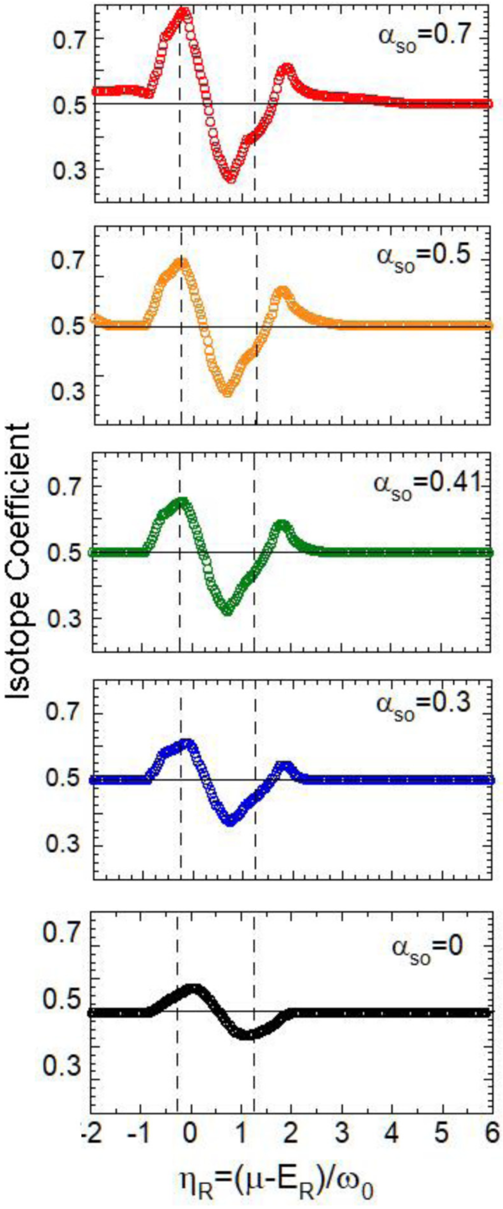

FIG. 15. Properties of the superconductive phase vs the Lifshitz parameter without and with RSOC for different α_{SO} values such that $\Delta E_{\mathrm{RSOC}} \gtreqless \Delta E_{2z}$. This figure shows the variation of the critical temperature with the cut-off energy via the isotope coefficient. The constant value predicted by the BCS theory is the black line.

As we have just seen, Figs. 10 and 13 clearly show a quantum resonance characterized by a Fano-type asymmetry in the superconducting parameters and a considerable deviation from the predictions of the BCS theory. To further highlight this last aspect we graph the isotopic coefficient $\gamma = \partial \ln T_C / \partial \ln M$ as a function of the rescaled Lifshitz parameter for different values of the parameter α_{SO}, assuming that the cut-off energy depend on the isotopic mass as $\omega_0 \propto M^{-1/2}$ [52,53] (Fig. 15).

In the BCS theory, the isotope coefficient has a constant value as the chemical potential changes to 0.5, in our case instead we notice a considerable deviation from this value when the rescaled Lifshitz parameter is in the range $0 < \eta_R < 1$ (for this range of values, the behavior of the γ parameter is typical of the Fano antiresonance), that is, when the system is close to a Lifshitz transition. These deviations from the BCS theory increase as the Rashba coupling α_{SO} increases, therefore there exists an unconventional dependence of the critical temperature on the cut-off energy unlike what is proposed in the BCS theory.

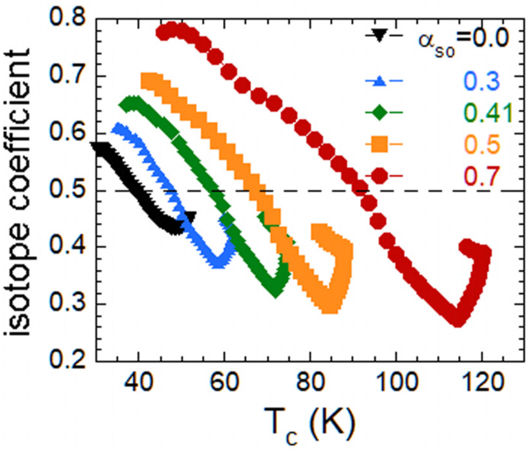

FIG. 16. The isotope coefficient as a function of the critical temperature for different values of α_{SO}.

In the high-energy limit, the gap ratio and the isotope coefficient tend to the values predicted by the BCS theory, so we are dealing with two BCS-like condensates.

In Fig. 16 we plot the isotope coefficient as a function of the critical temperature for different values of α_{SO} for the range of energies delimited in Fig. 15 by the dashed lines. This parameter, in this range of energies, can be measured and this prediction can be experimentally verified.

These results confirm that in correspondence with the van Hove singularity there is an amplification of the characteristic parameters of the superconductive phase which becomes more and more evident when the Rashba coupling exceeds a limit value of 0.4.

The works [36,42] investigated the superconducting properties for a superlattice of quantum wells and observed that there is an optimum condition for the amplification of the critical temperature that is obtained when the cut-off energy is equal to the dispersion along the confinement direction of the higher energy band. The particular geometry considered creates, in fact, a multicomponent system. Here, instead, by introducing the degree of freedom of spin in the solution of the Bogoliubov equations, as well as having the possibility of dealing with realistic cases, we can overcome the limit imposed by previous works simply by suitably increasing the Rashba coupling that exists by definition at the interface between different materials that make up a heterostructure.

V. CONCLUSIONS

The aim of this work has been to investigate theoretically and numerically the electronic structure and the superconducting properties of a nanostructured superlattice of quantum layers in the presence of RSOC. We have described the unconventional Lifshitz transition in a 3D superlattice of metallic layers characterized by the length of the circular nodal line increasing with RSOC in the negative helicity states of the spin-orbit split electron spectrum. Here we have provided the description of the tuning the multigap Bogoliubov superconductivity near the bottom of the upper subband with negative helicity shifted by the RSOC. Our theory overcomes the limitations present so far due to common BCS approximations used in previous theoretical works on superconductivity in the presence of spin-orbit interactions which mostly describe superconductivity only at very high Fermi energy. The work in Ref. [54] constitutes an important exception, focusing on superconductivity in low-density semimetals in the presence of strong spin-orbit coupling and analyzing the superconducting instability in different pairing channels. This latter work clearly shows the need to systematically develop the extension of the BCS theory in strongly spin-orbit coupled systems (see also [55]). We have shown the key role of the quantum configuration interaction between the gaps in the self-consistent mean-field equation which requires the calculation of the exchange interactions between singlet pairs in subbands with different quantum number and different helicity. The exchange interactions are key contact interactions which have been shown to be essential in condensation phenomena in fermionic quantum ultracold gases. In our theory the contact interactions are in action together with the phonon exchange cooper pairing. The key result of this work has been the calculation of the overlap of the electron wave.functions by solving the nonrelativistic Dirac equation. The results of this work provide a roadmap for the quantum material design of a superlattice of periodicity d made of superconducting atomic flakes of thickness L separated by spacers of thickness W where the energy dispersion in the transversal direction is of the order the pairing energy cutoff and the spin-orbit length is of the order of the 3D superlattice period. Resonant and crossover phenomena in the normal state are amplified when the transverse energy dispersion of electrons in the superlattice is of the same order of magnitude as the energy cutoff $\Delta E_z \sim \hbar\omega_0$ of the effective pairing interaction. Under these conditions the introduction of a RSOC creates a completely unexpected variation in the topology of the Fermi surface, especially for the negative helicity band. In particular, the RSOC induces an unconventional Lifshitz transition with an associated extended van Hove singularity. For the non-BCS superconducting phase we have solved the Bogoliubov equation for the multiple gaps numerically. The unusual complexity in the properties of the normal phase is reflected in an amplification of the gap and the critical temperature in precise energy ranges. We have found that the enhancement of the superconducting parameters takes place when the chemical potential is tuned around the Lifshitz transition. Under these circumstances it is necessary to include the configuration interaction between different gaps in different subbands.

The issue of superconducting fluctuations in a multiband and multigap configuration deserves a comment at this point. Whereas amplitude and phase fluctuations of the order parameter are in general detrimental and a source of large suppression of the (otherwise enhanced) critical temperature in low dimensional and/or strongly coupled superconductors, their effect can be reduced by the recently proposed mechanism [56,57] of the screening of superconducting fluctuations in a (at least) two-band system. References [56,57] demonstrated that a coexistence of a shallow carrier band with strong pairing and a deep band with weak pairing, together with the exchangelike pair transfer between the bands to couple the two condensates, realizes an optimal and robust multicomponent superconductivity regime: it preserves strong pairing to generate large gaps and a very high critical temperature but screens the detrimental superconducting fluctuations, thereby suppressing the pseudogap state. The screening is found to be very efficient even when the pair exchange is very small. Thus, a multiband superconductor with a coherent mixture of condensates in the BCS regime (deep band) and in the BCS-BEC crossover regime (shallow band) offers a promising route to enhance critical temperatures, eliminating at the same time the suppression effect due to fluctuations. In the light of these considerations, a quantitative calculation of the screening in the system here considered, requiring the inclusion of the spin-orbit coupling terms in the fluctuation propagator, is postponed to a future work. The coexistence of at least one large Fermi surface and at least one small Fermi surface appearing or disappearing with small changes in the chemical potential is the key ingredient for the shape resonance idea in superconducting gaps [35,36] which is a type of Fano-Feshbach resonance. By changing the chemical potential, the critical temperature (T_C) decreases towards 0 K when the chemical potential is tuned to the band edge, because of the Fano antiresonance, and the T_C maximum appears (as in Fano resonances) at higher energy, between one and two times the pairing interaction above the band edge [35,36,38]. Finally, one of the most interesting aspects highlighted by this work is the existence of an optimal condition for the amplification of the critical temperature when the band shift due to RSOC is larger than the dispersion along z of the upper subband and the cut-off energy.

ACKNOWLEDGMENTS

We gratefully thank Andrea Perali for discussions. We thank the staff of Department of Mathematics and Physics of Roma Tre University and Superstripes-onlus for support of this research project.

[1] Y. A. Bychkov and É. I. Rashba, Pis'ma Zh. Eksp. Teor. Fiz. **39**, 66 (1984) [JETP Lett. **39**, 78 (1984)].

[2] E. I. Rashba, Fiz. Tverd. Tela **2**, 1224 (1960) [Sov. Phys. Solid State **2**, 1109 (1960)].

[3] V. M. Ramaglia, D. Bercioux, V. Cataudella, G. De Filippis, C. Perroni, and F. Ventriglia, Eur. Phys. J. B **36**, 365 (2003).

[4] J. Zhang, H. Hu, X.-J. Liu, and H. Pu, in *Annual Review of Cold Atoms and Molecules* (World Scientific, Singapore, 2014), pp. 81–143.

[5] C. Perroni, D. Bercioux, V. M. Ramaglia, and V. Cataudella, J. Phys.: Condens. Matter **19**, 186227 (2007).

[6] V. M. Ramaglia, V. Cataudella, G. De Filippis, and C. A. Perroni, Phys. Rev. B **73**, 155328 (2006).

[7] S. Caprara, F. Peronaci, and M. Grilli, Phys. Rev. Lett. **109**, 196401 (2012).

[8] D. Bucheli, M. Grilli, F. Peronaci, G. Seibold, and S. Caprara, Phys. Rev. B **89**, 195448 (2014).

[9] S. Caprara, D. Bucheli, M. Grilli, J. Biscaras, N. Bergeal, S. Hurand, C. Feuillet-Palma, J. Lesueur, A. Rastogi, and R. Budhani, *Spin* (World Scientific, Singapore, 2014), Vol. 4, p. 1440004.

[10] C. R. Ast, J. Henk, A. Ernst, L. Moreschini, M. C. Falub, D. Pacilé, P. Bruno, K. Kern, and M. Grioni, Phys. Rev. Lett. **98**, 186807 (2007).

[11] M. Sakano, J. Miyawaki, A. Chainani, Y. Takata, T. Sonobe, T. Shimojima, M. Oura, S. Shin, M. S. Bahramy, R. Arita, N. Nagaosa, H. Murakawa, Y. Kaneko, Y. Tokura, and K. Ishizaka, Phys. Rev. B **86**, 085204 (2012).

[12] K. Ishizaka, M. Bahramy, H. Murakawa, M. Sakano, T. Shimojima, T. Sonobe, K. Koizumi, S. Shin, H. Miyahara, A. Kimura *et al.*, Nat. Mater. **10**, 521 (2011).

[13] M. Liebmann, C. Rinaldi, D. Di Sante, J. Kellner, C. Pauly, R. N. Wang, J. E. Boschker, A. Giussani, S. Bertoli, M. Cantoni *et al.*, Adv. Mater. **28**, 560 (2016).

[14] Y. Feng, Q. Jiang, B. Feng, M. Yang, T. Xu, W. Liu, X. Yang, M. Arita, E. F. Schwier, K. Shimada *et al.*, Nat. Commun. **10**, 4765 (2019).

[15] V. Brosco and C. Grimaldi, Phys. Rev. B **95**, 195164 (2017).

[16] L. P. Gor'kov and E. I. Rashba, Phys. Rev. Lett. **87**, 037004 (2001).

[17] A. V. Chaplik and L. I. Magarill, Phys. Rev. Lett. **96**, 126402 (2006).

[18] E. Cappelluti, C. Grimaldi, and F. Marsiglio, Phys. Rev. Lett. **98**, 167002 (2007).

[19] J. P. Vyasanakere and V. B. Shenoy, Phys. Rev. B **83**, 094515 (2011).

[20] S. Takei, C.-H. Lin, B. M. Anderson, and V. Galitski, Phys. Rev. A **85**, 023626 (2012).

[21] G. Goldstein, C. Aron, and C. Chamon, Phys. Rev. B **92**, 020504(R) (2015).

[22] J. Hutchinson, J. E. Hirsch, and F. Marsiglio, Phys. Rev. B **97**, 184513 (2018).

[23] H. Allami, O. A. Starykh, and D. A. Pesin, Phys. Rev. B **99**, 104505 (2019).

[24] D. Stornaiuolo, D. Massarotti, R. Di Capua, P. Lucignano, G. P. Pepe, M. Salluzzo, and F. Tafuri, Phys. Rev. B **95**, 140502(R) (2017).

[25] D. Massarotti, A. Miano, F. Tafuri, and D. Stornaiuolo, Supercond. Sci. Technol. **33**, 034007 (2020).

[26] P. K. Rout, E. Maniv, and Y. Dagan, Phys. Rev. Lett. **119**, 237002 (2017).

[27] A. Ptok, K. Rodríguez, and K. J. Kapcia, Phys. Rev. Mater. **2**, 024801 (2018).

[28] C. Liu, X. Yan, D. Jin, Y. Ma, H.-W. Hsiao, Y. Lin, T. M. Bretz-Sullivan, X. Zhou, J. Pearson, B. Fisher *et al.*, arXiv:2004.07416.

[29] R. Mori, P. B. Marshall, K. Ahadi, J. D. Denlinger, S. Stemmer, and A. Lanzara, Nat. Commun. **10**, 5534 (2019).

[30] K. Gotlieb, C.-Y. Lin, M. Serbyn, W. Zhang, C. L. Smallwood, C. Jozwiak, H. Eisaki, Z. Hussain, A. Vishwanath, and A. Lanzara, Science **362**, 1271 (2018).

[31] D. Stornaiuolo and F. Tafuri, in *Fundamentals and Frontiers of the Josephson Effect* (Springer, Berlin, 2019), pp. 275–337.

[32] R. Caruso, H. G. Ahmad, A. Pal, G. P. Pepe, D. Massarotti, M. G. Blamire, and F. Tafuri, in *EPJ Web of Conferences* (EDP Sciences, Les Ulis, France, 2020), Vol. 233, p. 05007.

[33] A. Valletta, A. Bianconi, A. Perali, and N. Saini, Z. Phys. B **104**, 707 (1997).

[34] A. Bianconi, A. Valletta, A. Perali, and N. L. Saini, Physica C **296**, 269 (1998).

[35] A. Bianconi, J. Supercond. **18**, 625 (2005).

[36] D. Innocenti, N. Poccia, A. Ricci, A. Valletta, S. Caprara, A. Perali, and A. Bianconi, Phys. Rev. B **82**, 184528 (2010).

[37] A. A. Shanenko, M. D. Croitoru, A. V. Vagov, V. M. Axt, A. Perali, and F. M. Peeters, Phys. Rev. A **86**, 033612 (2012).

[38] A. Bianconi, D. Innocenti, A. Valletta, and A. Perali, J. Phys.: Conf. Ser. **529**, 012007 (2014).

[39] T. Jarlborg and A. Bianconi, Sci. Rep. **6**, 24816 (2016).

[40] M. V. Mazziotti, A. Valletta, G. Campi, D. Innocenti, A. Perali, and A. Bianconi, Europhys. Lett. **118**, 37003 (2017).

[41] M. Cariglia, A. Vargas-Paredes, M. M. Doria, A. Bianconi, M. V. Milošević, and A. Perali, J. Supercond. Novel Magn. **29**, 3081 (2016).

[42] D. Innocenti, S. Caprara, N. Poccia, A. Ricci, A. Valletta, and A. Bianconi, Supercond. Sci. Technol. **24**, 015012 (2010).

[43] G. E. Volovik, Phys. Usp. **61**, 89 (2018).

[44] I. Lifshitz *et al.*, Zh. ETF. **38**, 1569 (1960) [Sov. Phys. JETP **11**, 1130 (1960)].

[45] Y. Uemura, Physica C **282**, 194 (1997).

[46] N. Andrenacci, A. Perali, P. Pieri, and G. C. Strinati, Phys. Rev. B **60**, 12410 (1999).

[47] A. Perali, P. Pieri, and G. C. Strinati, Phys. Rev. Lett. **93**, 100404 (2004).

[48] F. Pistolesi and G. C. Strinati, Phys. Rev. B **49**, 6356 (1994).

[49] A. Bussmann-Holder and A. Bianconi, Phys. Rev. B **67**, 132509 (2003).

[50] Y. Bang and H.-Y. Choi, Phys. Rev. B **78**, 134523 (2008).

[51] O. V. Dolgov, I. I. Mazin, D. Parker, and A. A. Golubov, Phys. Rev. B **79**, 060502(R) (2009).

[52] A. Perali, A. Valletta, G. Bardeiloni, A. Bianconi, A. Lanzara, and N. Saint, J. Supercond. **10**, 355 (1997).

[53] A. Perali, D. Innocenti, A. Valletta, and A. Bianconi, Supercond. Sci. Technol. **25**, 124002 (2012).

[54] L. Savary, J. Ruhman, J. W. F. Venderbos, L. Fu, and P. A. Lee, Phys. Rev. B **96**, 214514 (2017).

[55] P. M. R. Brydon, L. Wang, M. Weinert, and D. F. Agterberg, Phys. Rev. Lett. **116**, 177001 (2016).

[56] L. Salasnich, A. A. Shanenko, A. Vagov, J. A. Aguiar, and A. Perali, Phys. Rev. B **100**, 064510 (2019).

[57] T. T. Saraiva, P. J. F. Cavalcanti, A. Vagov, A. S. Vasenko, A. Perali, L. Dell'Anna, and A. A. Shanenko, Phys. Rev. Lett. **125**, 217003 (2020).